



Design and PI of PDD generator Deliverable 3.2.1

Agreement n.:	308974
Duration	November 2012 – October 2017
Co-ordinator:	DTU Wind



The research leading to these results has received funding from the European Community's Seventh Framework Programme FP7-ENERGY-2012-1-2STAGE under grant agreement No. 308974 (INNWIND.EU).

PROPRIETARY RIGHTS STATEMENT

This document contains information, which is proprietary to the "INNWIND.EU" Consortium. Neither this document nor the information contained herein shall be used, duplicated or communicated by any means to any third party, in whole or in parts, except with prior written consent of the "INNWIND.EU" consortium.

Document information

Document Name:	Final report, Deliverable 3.2.1
Document Number:	D3.2.1
Author:	Andreas Penzkofer, Kais Atallah
Document Type	Report
Dissemination level	PU
Review:	Henk Polinder
Date:	31.8.2015
WP:	3
Task:	Subtask 3.2.1
Approval:	Approved by WP Leader

TABLE OF CONTENTS

TABLE OF CONTENTS	3
1 INTRODUCTION.....	4
2 ANALYTICAL MODEL.....	5
2.1 Analytical model for the airgap and permanent magnet regions.....	6
2.2 Analytical models for the iron regions	10
2.2.1 Pole-piece regions.....	10
2.2.2 Stator regions.....	12
2.3 Numerical considerations.....	14
3 COMPARISON WITH FINITE ELEMENT FOR A MAGNETIC GEAR	15
4 COMPARISON WITH FINITE ELEMENT FOR A PSEUDO-DIRECT DRIVE.....	18
5 ELECTROMAGNETIC LOSS ANALYSIS.....	26
6 DESIGN AND OPTIMISATION PROCEDURE.....	29
6.1 Optimisation of the Magnetic Gear component for a 10MW wind turbine.....	29
6.2 Optimisation of the Pseudo-Direct Drive for a 10MW wind turbine	38
7 UP-SCALING TO 20MW	43
8 CONCLUSION	47
9 PUBLICATIONS RESULTING FROM THE WORK	48
APPENDIX A: ELECTRICAL PARAMETERS OF THE OPTIMISED 10MW PDD.....	49
APPENDIX B: ELECTRICAL PARAMETERS OF THE OPTIMISED 20MW PDD.....	51

1 INTRODUCTION

Pseudo-Direct Drives (PDD) offer an innovative alternative to Permanent magnet (PM) direct drives for wind turbines, Fig. 1. Since these machines have torque densities at least twice that of equivalent radial-field PM direct-drives machines, they may enable the realisation of light-weight and cost-effective wind-turbine drive train solutions [1]. However, key to achieving such a solution is the optimisation of the PDD, which so far has been performed by the use of finite element (FE) methods. While FE predictions may allow for an accurate analysis they also could result in a significant computational effort and therefore may not be a suitable tool for multi-dimensional design optimisation. Analytical models for electrical machines may offer a numerically fast yet accurate approach to design the PDD. However while many analytical models have been proposed for single airgap electrical machines [2], only few have discussed the topology of a magnetic gear (MG) [3]-[4] where two airgaps are present, while none have addressed the PDD prior to this project. In the framework of this project these models are further developed to account for the entire geometry of the active components of the PDD, including the iron regions of the pole-pieces (PP) and the stator. The predictions of the analytical models are compared to those from 2D FE, both on no-load and on-load operating conditions, and an excellent agreement is achieved as will be seen in the chapters 3 and 4. Procedures have been developed to optimise the MG and the PDD for wind turbine application and these are implemented into MATLAB. The developed code can readily be converted to other common languages, such as C++, and can be combined with a graphical user interface (GUI). The developed tool has been utilised to analyse and optimise PDDs for the power class of 10-20MW. Furthermore, FE studies have shown that adopting Halbach magnetization (HM) distributions results in significant improvement in the torque transmission capability of a MG [5]. A HM distribution also provides an inherently sinusoidal magnetic field, which allows for small torque ripple and a self-shielding magnetization that reduces the required back-iron and may result in a significantly higher airgap field than equivalent radially magnetized PMs. Therefore, the model presented also considers a Halbach magnetisation on both high-speed (HS) rotor and stator. Furthermore, the model is utilised to quantify and compare the effects of a radial magnetisation and a Halbach magnetisation on both HS rotor and stator.

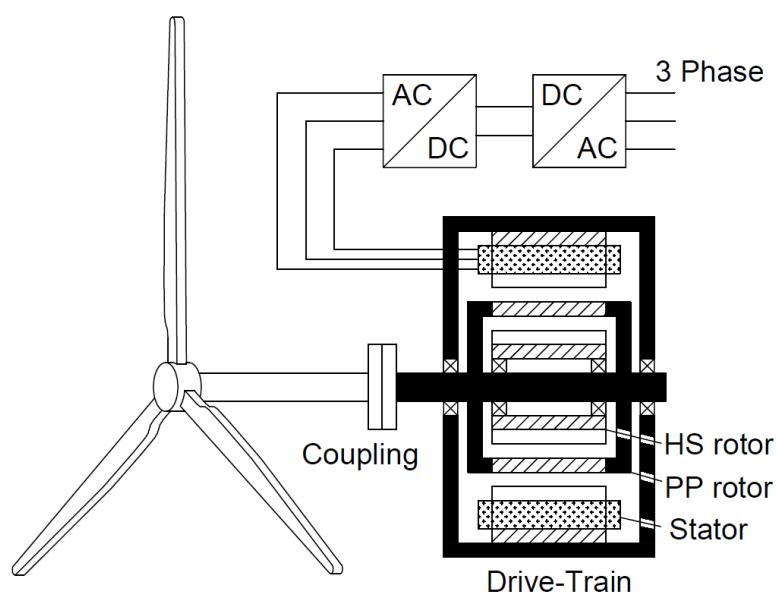


Fig. 1 Schematic for the integration of a PDD within a wind turbine.

2 ANALYTICAL MODEL

Analytical models for the prediction of the flux density distributions in the air, PM and lamination regions of a PDD for on-load conditions, considering radial and Halbach magnetisation, have been developed in this project [6]-[8]. Fig. 2 shows the schematic of a PDD and its various regions employed for the development of the analytical model. In the analysis the iron is assumed to be infinitely permeable and the end effects are neglected. The windings are represented by a current sheet at the stator iron bore radius R_S . Initially the solutions for the flux density distributions in the air and PM regions are derived and various secondary parameters, such as the torque and the shear stress are obtained from the predicted flux density distributions in the airgap regions. In order to calculate the iron losses in the lamination regions a detailed knowledge about the flux density distribution in the pole-piece (PP) iron regions and the average flux density distribution in the stator iron regions is required. Therefore, the solutions obtained for the magnetic flux density in the PM and air regions are utilised to compute the flux density distribution in the PP iron regions and the average flux density distributions in the stator iron regions. Furthermore, a model for the air and PM regions of a MG is readily available by setting the current sheet to zero.

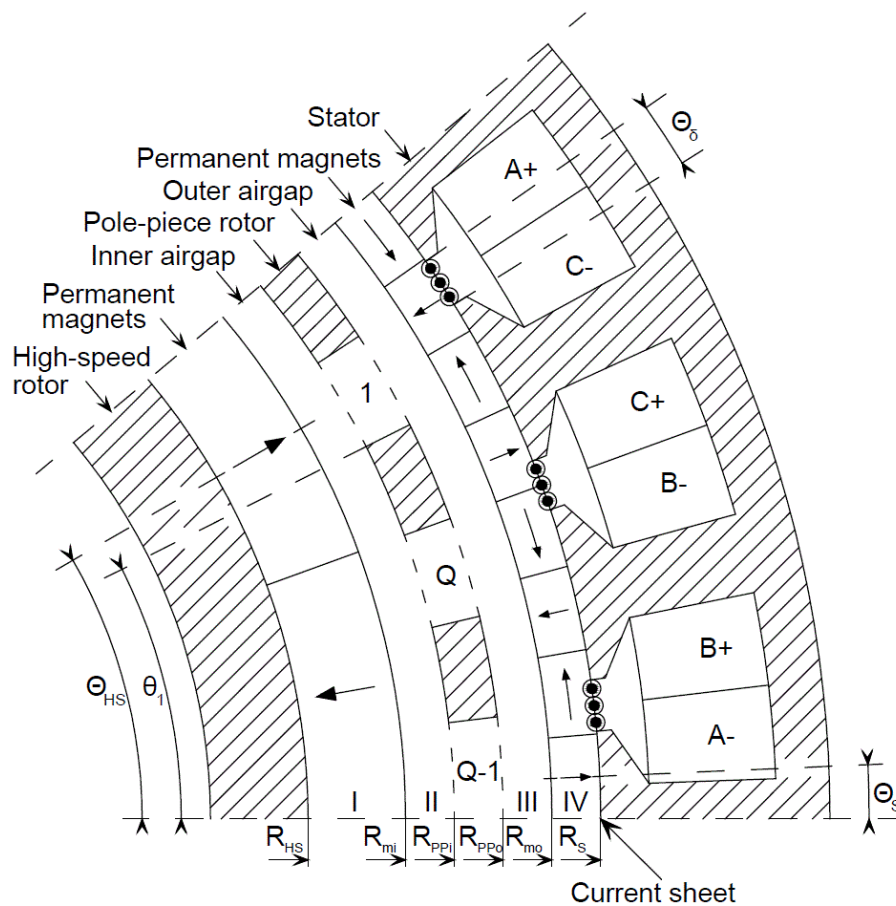


Fig. 2. Geometry for a PDD section. PMs consist of four Halbach segments per pole-pair on the stator. A current sheet is situated at the bore radius R_S .

2.1 Analytical model for the airgap and permanent magnet regions

For quasi-static conditions the Maxwell equations are

$$\nabla \vec{B} = 0 \quad (1)$$

$$\nabla \times \vec{H} = \vec{j} \quad (2)$$

where \vec{B} is the magnetic flux density, \vec{H} is the magnetic field strength, and \vec{j} is the current density. \vec{B} is related to \vec{H} by

$$\vec{B} = \mu_0 \vec{H} \quad \text{in air regions} \quad (3)$$

$$\vec{B} = \mu_0 \mu_r \vec{H} + \mu_0 \vec{M} \quad \text{in PM regions} \quad (4)$$

where \vec{M} is the residual magnetisation, μ_0 is the permeability of free space, and μ_r is the relative permeability of the PMs. The solution is obtained by solving the Laplace and Poisson equations

$$\Delta \vec{A} = 0 \quad \text{in air regions} \quad (5)$$

$$\Delta \vec{A} = -\mu_0 \nabla \times \vec{M} \quad \text{in PM regions} \quad (6)$$

and applying the boundary conditions, where \vec{A} is the vector potential and is related to the flux density by $\vec{B} = \nabla \times \vec{A}$. Since end effects are neglected only the z-component of \vec{A} is considered and it can be expressed as a Fourier series. The coefficients of the Fourier series for each region are related, and are determined by applying the boundary conditions at the interfaces and solving the resulting matrix equation. Viz. for the interfaces between air/PM regions and iron regions the tangential component of the magnetic field is set to zero. With the exception of the stator bore, where the tangential component of the magnetic field is set to be equal to the current sheet representing the stator windings. Furthermore, at all other interfaces the tangential component of the magnetic field and the normal component of the flux density are set to be equal [3]. At the stator bore radius R_s , the circumferential component of the magnetic field equals the current sheet, thus

$$H_{\theta,IV}(R_s, \theta) = \frac{B_{\theta,IV}(R_s, \theta)}{\mu_0 \mu_r} - \frac{M_{\theta,IV}(\theta)}{\mu_r} = -J_s(\theta) \quad (7)$$

where $H_{\theta,IV}$, $B_{\theta,IV}$ and $M_{\theta,IV}$ are the circumferential components of the magnetic field, flux density and residual magnetisation in region IV, respectively. J_s is the current sheet representing the stator windings and is expressed in form of a Fourier representation by the coefficients $J_{A,n}$ and $J_{B,n}$ as

$$J_s(\theta) = \sum_{n=1}^{\infty} \begin{pmatrix} J_{A,n} \\ J_{B,n} \end{pmatrix} \cdot \begin{pmatrix} \cos(n\theta) \\ \sin(n\theta) \end{pmatrix} \quad (8)$$

The solution for the vector potential in the magnet region IV is given by

$$A_{IV}(r, \theta) = A_{G,IV}(r, \theta) + A_{P,IV}(r, \theta) + A_{C,IV}(r, \theta) \quad (9)$$

where $A_{G,IV}$ and $A_{P,IV}$ are the general and a particular solution of equation (6) respectively when the current sheet is not considered, plus a term $A_{C,IV}$ that takes into account of the current sheet. Furthermore these can be expressed as

$$A_{G,IV}(r, \theta) = \sum_{n=1}^{\infty} \frac{P_n(r, R_S)}{P_n(R_{mo}, R_S)} \begin{pmatrix} A_{IV,n} \\ C_{IV,n} \end{pmatrix} \cdot \begin{pmatrix} \cos(n\theta) \\ \sin(n\theta) \end{pmatrix} \quad (10)$$

$$A_{P,IV}(r, \theta) = B_r \sum_{n=1}^{\infty} \begin{pmatrix} X_{IV,A,n}(r) \\ X_{IV,C,n}(r) \end{pmatrix} \cdot \begin{pmatrix} \cos(n\theta) \\ \sin(n\theta) \end{pmatrix} \quad (11)$$

$$A_{C,IV}(r, \theta) = \mu_0 \mu_r \sum_{n=1}^{\infty} \frac{R_S}{n} \left\{ \left(\frac{r}{R_S} \right)^n - \frac{P_n(r, R_S)}{P_n(R_{mo}, R_S)} \left(\frac{R_{mo}}{R_S} \right)^n \right\} \begin{pmatrix} J_{A,n} \\ J_{C,n} \end{pmatrix} \cdot \begin{pmatrix} \cos(n\theta) \\ \sin(n\theta) \end{pmatrix} \quad (12)$$

where B_r is the remanence of PMs, the radii R_{mo} and R_S are shown in Fig. 2, $A_{IV,n}$ and $C_{IV,n}$ are coefficients,

$$P_n(v, w) = \left(\frac{v}{w} \right)^n + \left(\frac{v}{w} \right)^{-n} \quad (13)$$

and v and w are variables. $X_{IV,A,n}(r)$ and $X_{IV,C,n}(r)$ are functions dependent on the magnetisation distribution, and for a discrete Halbach magnetisation distribution their expressions are given by [6]:

$$\begin{pmatrix} X_{IV,A,n}(r) \\ X_{IV,C,n}(r) \end{pmatrix} = X_{IV,n}(r) \begin{pmatrix} \sin(n\theta_S) \\ -\cos(n\theta_S) \end{pmatrix} \quad (14)$$

$$X_{IV,n}(r) = h_{n,m_S,p_S} \left(Y_{IV,n}(r) - \frac{P_n(r, R_S)}{P_n(R_{mo}, R_S)} Y_{IV,n}(R_{mo}) \right) \quad (15)$$

$$h_{n,m_S,p_S} = \frac{m_S p_S}{\pi} \frac{\sin\left(n \frac{\pi}{m_S p_S}\right)}{n} \epsilon_{n,p_S} \quad (16)$$

$$Y_{IV,n}(r) = \frac{R_S}{n} \left(\frac{r}{R_S} \right)^n G_{IV,n} + f_n(r) (n \epsilon_{n,m_S,p_S}^+ + \epsilon_{n,m_S,p_S}^-) \quad (17)$$

$$f_n(r) = \begin{cases} r \frac{1}{1-n^2} & n > 1 \\ \frac{1}{2} r \ln(r) & n = 1 \end{cases} \quad (18)$$

$$\epsilon_{n,m_S,p_S}^+ = \epsilon_{m_S p_S, n-p_S} + \epsilon_{m_S p_S, n+p_S} \quad (19)$$

$$\epsilon_{n,m_S,p_S}^- = \epsilon_{m_S p_S, n-p_S} - \epsilon_{m_S p_S, n+p_S} \quad (20)$$

$$G_{IV,n} = - (n \epsilon_{n,m_S,p_S}^+ + \epsilon_{n,m_S,p_S}^-) \frac{\partial f_n}{\partial r}(R_S) + \epsilon_{n,m_S,p_S}^- \quad (21)$$

$$\epsilon_{n,p_S} = \begin{cases} 1 & n \bmod p_S = 0 \\ 0 & n \bmod p_S \neq 0 \end{cases} \quad (22)$$

where p_S is the number of pole-pairs on the stator, m_S is the number of Halbach segments per pole-pair, θ_S is an angle depended on the position of the stator PMs, shown in Fig. 2, and $n \bmod p_S$ is the modulo operation. Similarly the solutions for PM region I are given by

$$A_I(r, \theta) = A_{G,I}(r, \theta) + A_{P,I}(r, \theta) \quad (23)$$

where

$$A_{G,I}(r, \theta) = \sum_{n=1}^{\infty} \frac{P_n(r, R_{HS})}{P_n(R_{mi}, R_{HS})} \begin{pmatrix} A_{I,n} \\ C_{I,n} \end{pmatrix} \cdot \begin{pmatrix} \cos(n\theta) \\ \sin(n\theta) \end{pmatrix} \quad (24)$$

$$A_{P,I}(r, \theta) = B_r \sum_{n=1}^{\infty} \begin{pmatrix} X_{I,A,n}(r) \\ X_{I,C,n}(r) \end{pmatrix} \cdot \begin{pmatrix} \cos(n\theta) \\ \sin(n\theta) \end{pmatrix} \quad (25)$$

$$\begin{pmatrix} X_{I,A,n}(r) \\ X_{I,C,n}(r) \end{pmatrix} = X_{I,n}(r) \begin{pmatrix} \sin(n\theta_{HS}) \\ -\cos(n\theta_{HS}) \end{pmatrix} \quad (26)$$

$$X_{I,n}(r) = h_{n,m_{HS},p_{HS}} \left(Y_{I,n}(r) - \frac{P_n(r, R_{HS})}{P_n(R_{mi}, R_{HS})} Y_{I,n}(R_{mo}) \right) \quad (27)$$

$$Y_{I,n}(r) = \frac{R_{HS}}{n} \left(\frac{r}{R_{HS}} \right)^n G_{I,n} + f_n(r) (n\epsilon_{n,m_{HS},p_{HS}}^+ + \epsilon_{n,m_{HS},p_{HS}}^-) \quad (28)$$

$$G_{I,n} = -(n\epsilon_{n,m_{HS},p_{HS}}^+ + \epsilon_{n,m_{HS},p_{HS}}^-) \frac{\partial f_n}{\partial r}(R_{HS}) + \epsilon_{n,m_{HS},p_{HS}}^- \quad (29)$$

the radii R_{HS} and R_{mi} are shown in Fig. 2, and $A_{I,n}$ and $C_{IV,n}$ are coefficients. The form of the solutions in regions II, III and the PP air regions I,...,Q are given by [3]:

$$A_{II}(r, \theta) = A_{II,0} + \sum_{n=1}^{\infty} \left\{ \frac{R_{mi}}{n} \frac{P_n(r, R_{PPi})}{E_n(R_{mi}, R_{PPi})} \begin{pmatrix} A_{II,n} \\ C_{II,n} \end{pmatrix} + \frac{R_{PPi}}{n} \frac{P_n(r, R_{mi})}{E_n(R_{PPi}, R_{mi})} \begin{pmatrix} B_{II,n} \\ D_{II,n} \end{pmatrix} \right\} \cdot \begin{pmatrix} \cos(n\theta) \\ \sin(n\theta) \end{pmatrix} \quad (30)$$

$$A_{III}(r, \theta) = A_{III,0} + \sum_{n=1}^{\infty} \left\{ \frac{R_{PPo}}{n} \frac{P_n(r, R_{mo})}{E_n(R_{PPo}, R_{mo})} \begin{pmatrix} A_{III,n} \\ C_{III,n} \end{pmatrix} + \frac{R_{mo}}{n} \frac{P_n(r, R_{PPo})}{E_n(R_{mo}, R_{PPo})} \begin{pmatrix} B_{III,n} \\ D_{III,n} \end{pmatrix} \right\} \cdot \begin{pmatrix} \cos(n\theta) \\ \sin(n\theta) \end{pmatrix} \quad (31)$$

$$A_i(r, \theta) = A_{i,0} + B_{i,0} \ln r + \sum_{n=1}^{\infty} \left\{ \frac{E_{n\pi/\beta}(r, R_{PPo})}{E_{n\pi/\beta}(R_{PPi}, R_{PPo})} A_{i,n} + \frac{E_{n\pi/\beta}(r, R_{PPi})}{E_{n\pi/\beta}(R_{PPi}, R_{PPo})} B_{i,n} \right\} \cos\left(\frac{n\pi}{\beta}(\theta - \theta_i)\right) \quad (32)$$

where $A_{II,n}$, $B_{II,n}$, $C_{II,n}$, $D_{II,n}$, $A_{III,n}$, $B_{III,n}$, $C_{III,n}$, $D_{III,n}$, $A_{i,n}$, $B_{i,n}$, $A_{i,0}$, and $B_{i,0}$ are coefficients, β is the PP slot opening angle, the radii R_{PPi} and R_{PPo} are shown in Fig. 2,

$$E_n(v, w) = \left(\frac{v}{w}\right)^n - \left(\frac{v}{w}\right)^{-n} \quad (33)$$

and v and w are variables. Applying the boundary conditions at the interface between region III and IV:

$$B_{rad,III}(R_{mo}, \theta) = B_{rad,IV}(R_{mo}, \theta) \quad (34)$$

$$B_{\theta,III}(R_{mo}, \theta) = \frac{B_{\theta,IV}(R_{mo}, \theta)}{\mu_r} - \frac{\mu_0 M_{\theta,IV}(\theta)}{\mu_r} \quad (35)$$

gives the following relations between coefficients of regions III and IV for a discrete Halbach magnetisation [6]:

$$\begin{pmatrix} A_{IV,n} \\ C_{IV,n} \end{pmatrix} = \begin{pmatrix} B_{III,n} \\ D_{III,n} \end{pmatrix} \frac{R_{mo}}{n} \frac{P_n(R_{mo}, R_{PPo})}{E_n(R_{mo}, R_{PPo})} + \begin{pmatrix} A_{III,n} \\ C_{III,n} \end{pmatrix} \frac{R_{PPo}}{n} \frac{2}{E_n(R_{PPo}, R_{mo})} \quad (36)$$

$$\begin{pmatrix} B_{III,n} \\ D_{III,n} \end{pmatrix} = \frac{n}{\mu_r R_{mo}} \begin{pmatrix} A_{IV,n} \\ C_{IV,n} \end{pmatrix} \frac{E_n(R_{mo}, R_S)}{P_n(R_{mo}, R_S)} + \mu_0 \left(\frac{R_{mo}}{R_S} \right)^{n-1} \left\{ 1 - \frac{E_n(R_{mo}, R_S)}{P_n(R_{mo}, R_S)} \right\} \begin{pmatrix} J_{A,n} \\ J_{C,n} \end{pmatrix} \quad (37)$$

$$+ \frac{B_r}{\mu_r} (-h_{n,m_S,p_S} \epsilon_{n,m_S,p_S}^- + X'_{IV,n}(R_{mo})) \begin{pmatrix} \sin(n\theta_S) \\ -\cos(n\theta_S) \end{pmatrix}$$

where the radius R_{PPo} is shown in Fig. 1, $X'_{IV,n}(r)$ is the derivative of $X_{IV,n}(r)$. Similarly the relations of coefficients between regions I and II are given by

$$\begin{pmatrix} A_{I,n} \\ C_{I,n} \end{pmatrix} = \begin{pmatrix} A_{II,n} \\ C_{II,n} \end{pmatrix} \frac{R_{mi}}{n} \frac{P_n(R_{mi}, R_{PPi})}{E_n(R_{mi}, R_{PPi})} + \begin{pmatrix} B_{II,n} \\ D_{II,n} \end{pmatrix} \frac{R_{PPi}}{n} \frac{2}{E_n(R_{PPi}, R_{mi})} \quad (38)$$

$$\begin{pmatrix} A_{II,n} \\ C_{II,n} \end{pmatrix} = \frac{n}{\mu_r R_{mi}} \begin{pmatrix} A_{I,n} \\ C_{I,n} \end{pmatrix} \frac{E_n(R_{mi}, R_{HS})}{P_n(R_{mi}, R_{HS})} \quad (39)$$

$$+ \frac{B_r}{\mu_r} (-h_{n,m_{HS},p_{HS}} \epsilon_{n,m_{HS},p_{HS}}^- + X'_{I,n}(R_{mi})) \begin{pmatrix} \sin(n\theta_{HS}) \\ -\cos(n\theta_{HS}) \end{pmatrix}$$

The relations between coefficients of region II, III and 1, ..., Q are given by [3]:

$$\begin{pmatrix} B_{II,n} \\ D_{II,n} \end{pmatrix} = \sum_{i=1}^Q \left\{ \frac{B_{i,0}}{\pi R_{PPi}} \begin{pmatrix} r(n, i) \\ s(n, i) \end{pmatrix} \right. \quad (40)$$

$$\left. + \sum_{k=1}^{\infty} \frac{k}{\beta R_{PPi}} \left[\frac{P_{k\pi/\beta}(R_{PPi}, R_{PPo})}{E_{k\pi/\beta}(R_{PPi}, R_{PPo})} A_{i,k} - \frac{2}{E_{k\pi/\beta}(R_{PPi}, R_{PPo})} B_{i,k} \right] \begin{pmatrix} f(k, n, i) \\ g(k, n, i) \end{pmatrix} \right\}$$

$$\begin{pmatrix} A_{III,n} \\ C_{III,n} \end{pmatrix} = \sum_{i=1}^Q \left\{ \frac{B_{i,0}}{\pi R_{PPo}} \begin{pmatrix} r(n, i) \\ s(n, i) \end{pmatrix} \right. \quad (41)$$

$$\left. + \sum_{k=1}^{\infty} \frac{k}{\beta R_{PPo}} \left[\frac{P_{k\pi/\beta}(R_{PPo}, R_{PPi})}{E_{k\pi/\beta}(R_{PPi}, R_{PPo})} A_{i,k} - \frac{2}{E_{k\pi/\beta}(R_{PPi}, R_{PPo})} B_{i,k} \right] \begin{pmatrix} f(k, n, i) \\ g(k, n, i) \end{pmatrix} \right\}$$

$$A_{i,k} = \sum_{n=1}^{\infty} \frac{2}{n\beta} \left\{ R_{mi} \frac{2}{E_n(R_{mi}, R_{PPi})} \begin{pmatrix} A_{II,n} \\ C_{II,n} \end{pmatrix} - R_{PPi} \frac{P_n(R_{mi}, R_{PPi})}{E_n(R_{mi}, R_{PPi})} \begin{pmatrix} B_{II,n} \\ D_{II,n} \end{pmatrix} \right\} \cdot \begin{pmatrix} f(k, n, i) \\ g(k, n, i) \end{pmatrix} \quad (42)$$

$$B_{i,k} = \sum_{n=1}^{\infty} \frac{2}{n\beta} \left\{ R_{PPo} \frac{P_n(R_{PPo}, R_{mo})}{E_n(R_{PPo}, R_{mo})} \begin{pmatrix} A_{III,n} \\ C_{III,n} \end{pmatrix} - R_{mo} \frac{2}{E_n(R_{PPo}, R_{mo})} \begin{pmatrix} B_{II,n} \\ D_{II,n} \end{pmatrix} \right\} \cdot \begin{pmatrix} f(k, n, i) \\ g(k, n, i) \end{pmatrix} \quad (43)$$

$$A_{i,0} + B_{i,0} \ln R_{PPi} = A_{II,0} + \sum_{n=1}^{\infty} \frac{2}{n\beta} \left\{ R_{mi} \frac{2}{E_n(R_{mi}, R_{PPi})} \begin{pmatrix} A_{II,n} \\ C_{II,n} \end{pmatrix} \right. \quad (44)$$

$$\left. - R_{PPi} \frac{P_n(R_{mi}, R_{PPi})}{E_n(R_{mi}, R_{PPi})} \begin{pmatrix} B_{II,n} \\ D_{II,n} \end{pmatrix} \right\} \cdot \begin{pmatrix} r(n, i) \\ s(n, i) \end{pmatrix}$$

$$A_{i,0} + B_{i,0} \ln R_{PPo} = A_{III,0} + \sum_{n=1}^{\infty} \frac{2}{n\beta} \left\{ R_{PPo} \frac{P_n(R_{PPo}, R_{mo})}{E_n(R_{PPo}, R_{mo})} \begin{pmatrix} A_{III,n} \\ C_{III,n} \end{pmatrix} \right. \quad (45)$$

$$-R_{mo} \frac{2}{E_n(R_{ppo}, R_{mo})} \left(\frac{B_{III,n}}{D_{III,n}} \right) \cdot \begin{pmatrix} r(n, i) \\ s(n, i) \end{pmatrix}$$

where $f(k, n, i)$, $g(k, n, i)$, $r(n, i)$ and $s(n, i)$ are functions given in [3].

The electromagnetic torque in the airgap regions is acquired by using the Maxwell stress tensor and integrating over a circle at a radius r within the airgap regions: The torque in the inner airgap is given by [3]:

$$\begin{aligned} T_i &= \frac{l_a R_i^2}{\mu_0} \int_0^{2\pi} B_{rad}(R_i, \theta) B_\theta(R_i, \theta) d\theta \\ &= \frac{\pi l_a R_i^2}{\mu_0} \sum_{n=1}^{\infty} (W_{II,1,n} W_{II,2,n} + W_{II,3,n} W_{II,4,n}) \end{aligned} \quad (46)$$

Where R_{mi} is the airgap radius and

$$W_{II,1,n} = -A_{II,n} \frac{R_{mi}}{R_i} \frac{P_n(R_i, R_{ppi})}{E_n(R_{mi}, R_{ppi})} - B_{II,n} \frac{R_{ppi}}{R_i} \frac{P_n(R_i, R_{mi})}{E_n(R_{ppi}, R_{mi})} \quad (47)$$

$$W_{II,2,n} = -C_{II,n} \frac{R_{mi}}{R_i} \frac{E_n(R_i, R_{ppi})}{E_n(R_{mi}, R_{ppi})} - D_{II,n} \frac{R_{ppi}}{R_i} \frac{E_n(R_i, R_{mi})}{E_n(R_{ppi}, R_{mi})} \quad (48)$$

$$W_{II,3,n} = C_{II,n} \frac{R_{mi}}{R_i} \frac{P_n(R_i, R_{ppi})}{E_n(R_{mi}, R_{ppi})} + D_{II,n} \frac{R_{ppi}}{R_i} \frac{P_n(R_i, R_{mi})}{E_n(R_{ppi}, R_{mi})} \quad (49)$$

$$W_{II,4,n} = -A_{II,n} \frac{R_{mi}}{R_i} \frac{E_n(R_i, R_{ppi})}{E_n(R_{mi}, R_{ppi})} - B_{II,n} \frac{R_{ppi}}{R_i} \frac{E_n(R_i, R_{mi})}{E_n(R_{ppi}, R_{mi})} \quad (50)$$

A similar set of expressions can be derived for the electromagnetic torque in the outer airgap.

2.2 Analytical models for the iron regions

Although the solution in the air and PM regions is sufficient for the accurate prediction of the transmitted average torque and torque ripple, the flux density distribution in the iron regions is required for the accurate prediction of the iron losses. Therefore, in this section, analytical models for the prediction of the flux density distribution in the PPs regions and the stator core are developed.

2.2.1 Pole-piece regions

Due to the complexity of the flux density distribution in the PPs a representation through average values in radial or circumferential directions may not be accurate. Therefore, a model which provides the flux density distribution in the PPs is developed. Furthermore, in large PDDs the radial dimensions and circumferential dimensions of the PPs are very small compared to the airgap diameters. Therefore, for simplicity a Cartesian coordinate system is employed, Fig. 3.

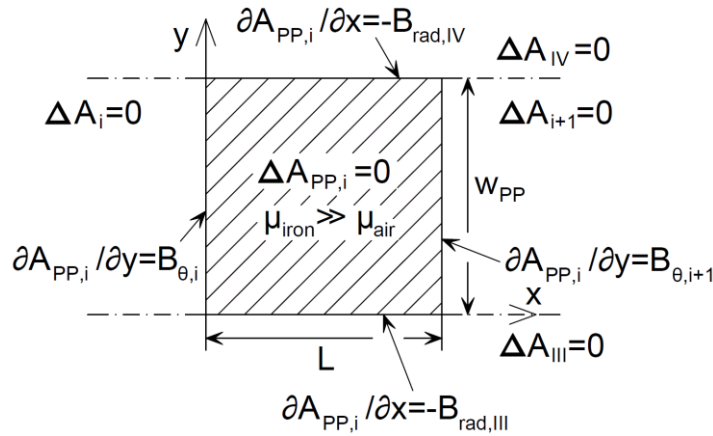


Fig. 3. Approximated geometry and boundary conditions for a PP in Cartesian coordinates.

x and y are the local Cartesian coordinates on one PP as shown in Fig. 3, with

$$x = (\theta - \theta_i)(R_{PPi} + R_{PPo})/2 = (\theta - \theta_i)R_{PPm} \quad (51)$$

$$y = r - R_{PPi} \quad (52)$$

where R_{PPm} is the mean radius of the PPs, θ_i is the angular position of the i -th PP, and the radii R_{PPi} and R_{PPo} are shown in Fig. 2. The average circumferential dimension of a PP is given by

$$L = \theta_{PP}(R_{PPi} + R_{PPo})/2 \quad (53)$$

where θ_{PP} is the angular dimension of a PP. Assuming the PPs having a constant permeability $\mu_{iron} \gg \mu_{air}$, the vector potential in the PPs satisfy the Laplace equation:

$$\Delta \vec{A}_{PP,i} = 0 \quad (54)$$

which can be solved applying the boundary conditions, that are determined by the magnetic field distributions derived in section II. Similarly to the solution in the air and PM regions only the z -component is considered. It is proposed, that the solution for the i -th PP is given by

$$A_{PP,i}(x, y) = A_{x1}(x, y) + A_{x2}(x, y) + A_{y1}(x, y) + A_{y2}(x, y) + A_0(x, y) \quad (55)$$

where

$$A_{x1}(x, y) = \sum_{n=1}^{\infty} a_{x1,n} \sinh\left(\frac{n\pi[L-x]}{W_{PP}}\right) \sin\left(\frac{n\pi y}{W_{PP}}\right) \quad (56)$$

$$A_{x2}(x, y) = \sum_{n=1}^{\infty} a_{x2,n} \sinh\left(\frac{n\pi x}{W_{PP}}\right) \sin\left(\frac{n\pi y}{W_{PP}}\right) \quad (57)$$

$$A_{y1}(x, y) = \sum_{n=1}^{\infty} a_{y1,n} \sin\left(\frac{n\pi x}{L}\right) \sinh\left(\frac{n\pi[W_{PP}-y]}{L}\right) \quad (58)$$

$$A_{y2}(x, y) = \sum_{n=1}^{\infty} a_{y2,n} \sin\left(\frac{n\pi x}{L}\right) \sinh\left(\frac{n\pi y}{L}\right) \quad (59)$$

$$A_0(x, y) = a_{x0}x + a_{y0}y + a_{xy}xy \quad (60)$$

where w_{PP} is the radial dimension of a PP. $a_{x1,n}$, $a_{x2,n}$, $a_{y1,n}$, $a_{y2,n}$, a_{x0} , a_{y0} and a_{xy} are coefficients, which are determined by applying the boundary conditions at the interfaces between iron and air regions:

$$\partial A_{PP,i}(0, y)/\partial y = B_{\theta}(R_{PPi} + y, \theta_i) \quad (61)$$

$$\partial A_{PP,i}(L, y)/\partial y = B_{\theta}(R_{PPi} + y, \theta_i + \theta_{PP}) \quad (62)$$

$$\partial A_{PP,i}(x, 0)/\partial x = -B_{rad}(R_{PPi}, \theta_i + x/R_{PPm}) \quad (63)$$

$$\partial A_{PP,i}(x, w_{PP})/\partial x = -B_{rad}(R_{PPo}, \theta_i + x/R_{PPm}) \quad (64)$$

The coefficients are then given by

$$a_{x1,n} = \frac{1}{n\pi} \int_0^{w_{PP}} \frac{\cos(n\pi y/w_{PP})}{\sinh(n\pi L/w_{PP})} \frac{\partial A_{PP,i}(0, y)}{\partial y} dy \quad (65)$$

$$a_{x2,n} = \frac{1}{n\pi} \int_0^{w_{PP}} \frac{\cos(n\pi y/w_{PP})}{\sinh(n\pi L/w_{PP})} \frac{\partial A_{PP,i}(L, y)}{\partial y} dy \quad (66)$$

$$a_{y1,n} = \frac{1}{n\pi} \int_0^L \frac{\cos(n\pi x/L)}{\sinh(n\pi w_{PP}/L)} \frac{\partial A_{PP,i}(x, 0)}{\partial x} dx \quad (67)$$

$$a_{y2,n} = \frac{1}{n\pi} \int_0^L \frac{\cos(n\pi x/L)}{\sinh(n\pi w_{PP}/L)} \frac{\partial A_{PP,i}(x, w_{PP})}{\partial x} dx \quad (68)$$

$$a_{x0} = \frac{1}{L} \int_0^L \frac{\partial A_{PP,i}(x, 0)}{\partial x} dx \quad (69)$$

$$a_{y0} = \frac{1}{w_{PP}} \int_0^{w_{PP}} \frac{\partial A_{PP,i}(0, y)}{\partial y} dy \quad (70)$$

$$a_{xy} = \frac{1}{Lw_{PP}} \int_0^{w_{PP}} \left[\frac{\partial A_{PP,i}(L, y)}{\partial y} - \frac{\partial A_{PP,i}(0, y)}{\partial y} \right] dy \quad (71)$$

2.2.2 Stator regions

The solution for the flux density distribution at the stator bore radius R_S , obtained from the analysis in section II, is employed to predict the average flux densities in the stator regions, viz. tooth tip, tooth body and back-iron, as shown in Fig. 4.

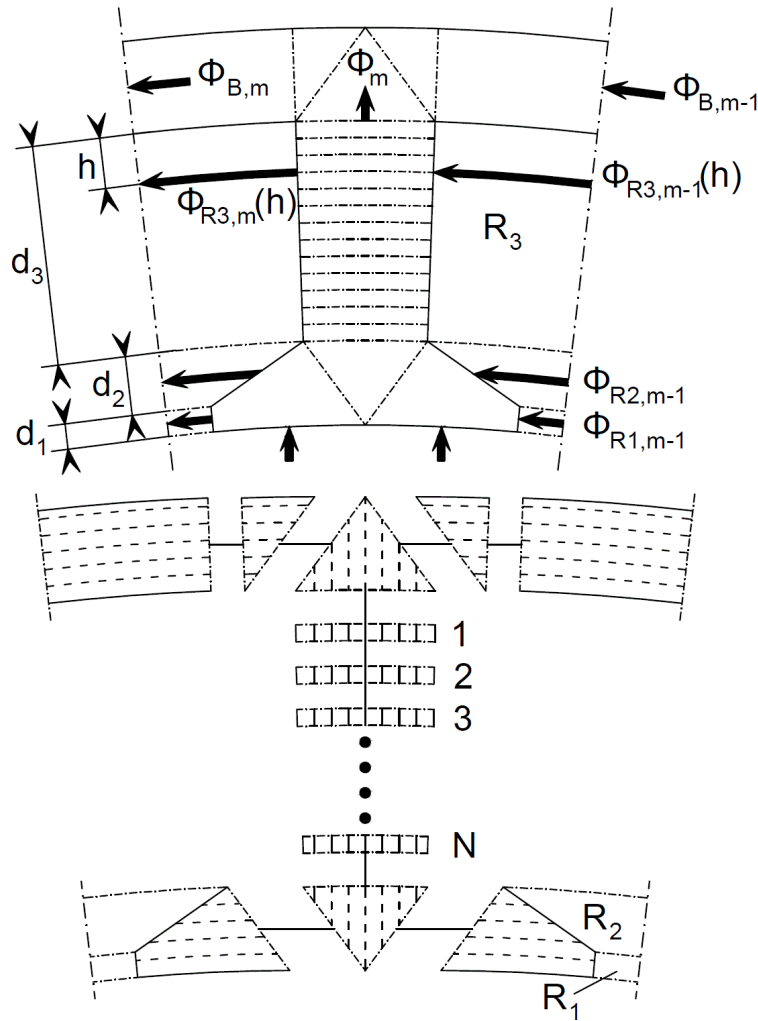


Fig. 4. Division of one tooth segment for the analysis in section 2.2.2. Assumed flux paths are shown as arrows for entering and exiting flux paths to and from the segment (above figure) and as dashed lines within the laminations (bottom figure).

Since the value of the average flux density varies along the radial direction of a tooth, especially on load, each tooth is split into N layers of radial thickness Δh . The flux due to the stator winding through region R1 and through region R3 is given by

$$\Phi_{R1,m} = \mu_0 \frac{I_{sl,m}}{w_1} d_1 l_a \quad \text{in region R1} \quad (72)$$

$$\Phi_{R3,m}(h) = \mu_0 \frac{I_{sl,m}}{w_2} \frac{h}{d_3} \Delta h l_a \quad \text{in region R3} \quad (73)$$

where $I_{sl,m}$ is the current in the m -th slot, w_1 is the slot opening and w_2 is the average slot width, l_a is the active axial length, and d_1 , d_2 , d_3 and h are dimensions shown in Fig. 4. The magnetic field strength across region R2 is deduced by averaging the field strength in region R1 and the field strength calculated at the bottom of the tooth. The flux across region R2 is then given by

$$\Phi_{R2,m} = \mu_0 \frac{l_{sl,m}}{w_1} \frac{1}{2} (1 + w_1/w_2) d_2 l_a \quad \text{in region } R_2 \quad (74)$$

The flux in the back-iron is given by [9]

$$\Phi_{B,1} = -\frac{1}{M} \sum_{k=1}^{M-1} (M-k) \Phi_{1+k} \quad (75)$$

$$\Phi_{B,M} = \frac{1}{M} \sum_{k=1}^{M-1} (M-k) \Phi_{M-k+1} \quad (76)$$

$$\Phi_{B,m} = \frac{1}{M} \sum_{k=1}^{m-1} (m-k) \Phi_{m-k+1} - \frac{1}{M} \sum_{k=1}^{M-m} (M-m-k+1) \Phi_{m+k} \quad (77)$$

where Φ_m is the flux at the end of the m -th tooth, $\Phi_{B,m}$ is the flux in the back-iron adjacent to the m -th tooth, and M is the total number of teeth for one section.

2.3 Numerical considerations

The analytical solutions in the airgap and magnet regions are computed with a finite number of Fourier series components. Taking into account the number of coefficients to be determined the size of the matrix to be inverted is $N_{total} \times N_{total}$, where $N_{total} = 12N + (2N_q + 2)Q$, where N is the highest order harmonic to be considered in regions I, II, III, and IV, and N_q is the highest order harmonic to be considered in the regions representing the air spaces between the PPs. In order to achieve an adequate accuracy N must be larger than the largest number of PM pole pairs in the MG. Therefore, for MGs equipped with a large number of poles, which would also have a large number of pole-pieces Q , N_{total} can be very large.

Due to the large size of the PDD it might be built from S circumferentially identical sections. Therefore, the analytical solution can be improved by taking into account of the circumferential symmetry. Any function f of the form

$$f(r, \theta) = \sum_{n=1}^N R_n(r) (a_n \cos(n\theta) + b_n \sin(n\theta)) \quad (78)$$

with a periodicity of $2\pi/S$, where $R_n(r)$ is a function of r , and a_n and b_n are coefficients, can be reduced to

$$f(r, \theta) = \sum_{j=S}^{N_{eff}S} R_j(r) (a_j \cos(j\theta) + b_j \sin(j\theta)) \quad (79)$$

where N_{eff} is the next lower integer to N/S and j is multiples of S . In addition, the number of boundary conditions related to the Q pole-piece rotor air regions are also reduced by a factor of S . Therefore, the total number of coefficients is reduced by a factor of S , and the dimensions of the matrix to be inverted are reduced by S^2 .

3 COMPARISON WITH FINITE ELEMENT FOR A MAGNETIC GEAR

Table I gives the parameters of a MG, which has been designed to meet the requirements of a 10MW wind turbine, and where the turbine is directly connected to the PP rotor. The analytical models have been compared with magneto-static FE analysis using the design specified in Table I.

TABLE I
Parameters of 10MW Magnetic Gear

Symbol	Quantity	Value
	Rated torque on the PP rotor	9.9 MNm
	Analytical pullout torque of the MG	11.9 MNm
G	Gear ratio	7.5
p_{HS}^*	Pole-pairs on HS rotor per section	2
p_S^*	Pole-pairs on stator per section	13
m_S	Halbach segments per pole-pair on the stator	4
Q^*	Pole-pieces per section	15
S	Number of identical sections	20
	PP slot opening angle	$\pi/300$ rad
D	Airgap diameter	6.0 m
w_{PP}	Radial thickness of PPs	31.4 mm
	Radial thickness of HS rotor PMs	39.8 mm
	Radial thickness of stator PMs	25.2 mm
	Length of inner airgap	6.0 mm
	Length of outer airgap	6.0 mm
l_a	Active axial length	1.66 m
	HS rotor pole arc to pole pitch ratio	0.8
B_r	Remanence of N48SH PMs at 100°C	1.25 T
μ_r	Relative recoil permeability of PMs	1.05

Fig. 5-Fig. 6 compare the analytical and finite element (FE) predicted radial components of the flux density in the airgaps of the MG element of the MG. It can be seen, that a very good agreement exists. Fig. 7-Fig. 8 compare the transmitted torque on the PP rotor and HS rotor and it can be seen a very good agreement exists between the analytical and FE predictions.

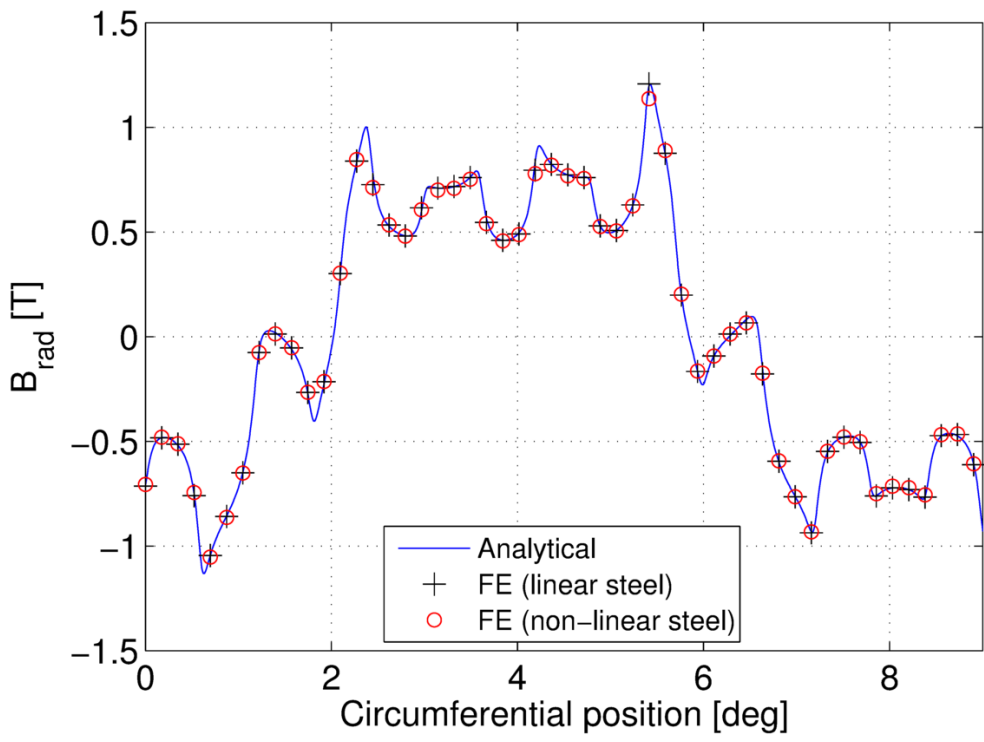


Fig. 5. Radial flux density in the inner airgap.

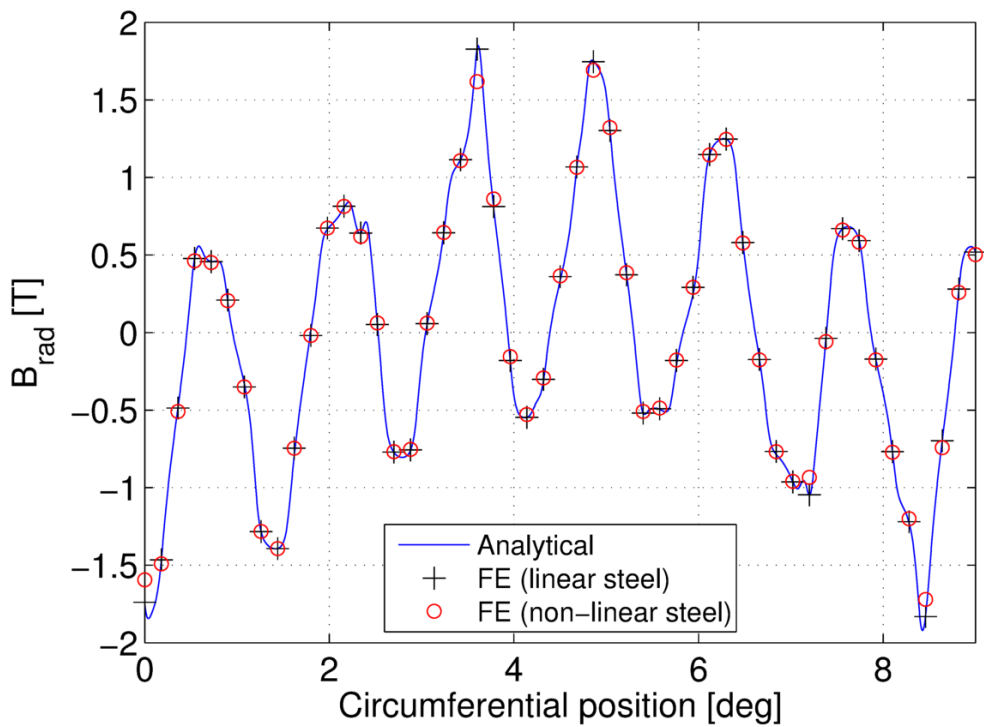


Fig. 6. Radial flux density in the outer airgap.

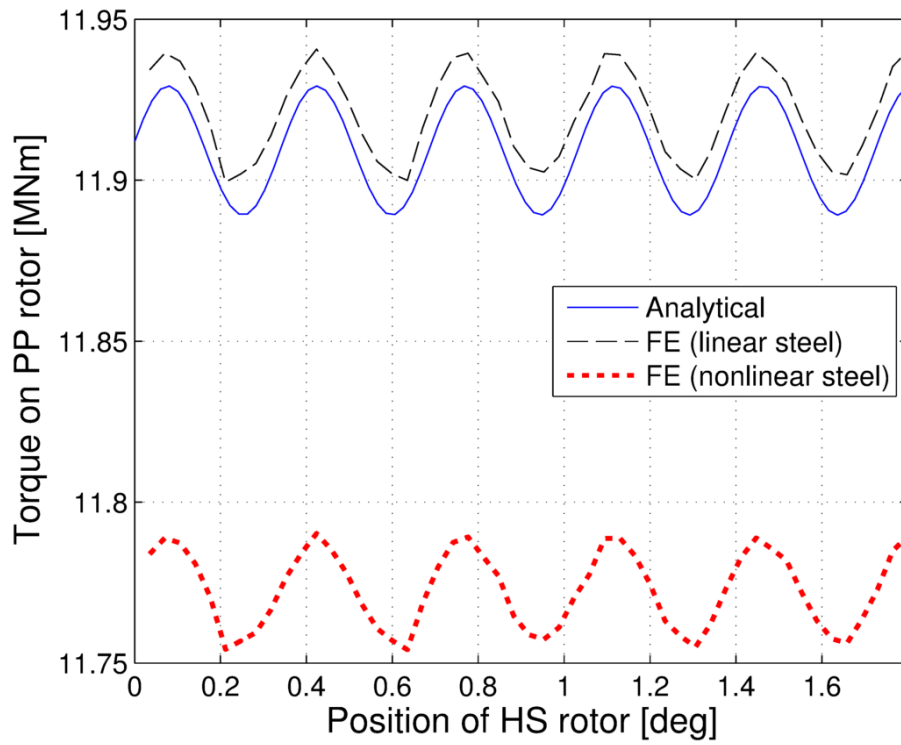


Fig. 7. Variation of transmitted torque on the PP rotor with the position.

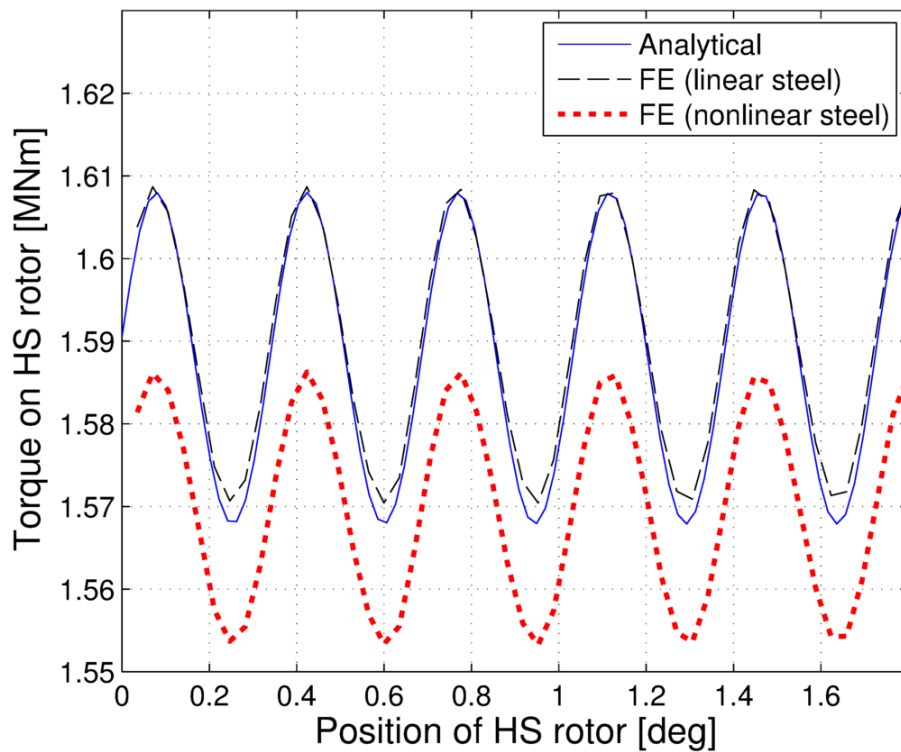


Fig. 8. Variation of transmitted torque on the HS rotor with the position.

4 COMPARISON WITH FINITE ELEMENT FOR A PSEUDO-DIRECT DRIVE

Table II gives the parameters of a 10MW PDD, which have been designed to meet the requirements of a 10MW wind turbine, and where the turbine is directly connected to the PP rotor. The analytical models have been compared with magneto-static FE analysis using the design specified in Table II.

TABLE II
Parameters of 10MW PDD

Symbol	Quantity	Value
	Rated power	10 MW
$\Omega_{PP,R}$	Rated speed of PP rotor	9.65 rpm
	Rated torque on the PP rotor	9.9 MNm
	Analytical pullout torque of the MG	11.9 MNm
$f_{out,R}$	Rated electrical output frequency	48.25 Hz
G	Gear ratio	7.5
p_{HS}^*	Pole-pairs on HS rotor per section	2
p_S^*	Pole-pairs on stator per section	13
m_S	Halbach segments per pole-pair on the stator	4
Q^*	Pole-pieces per section	15
S	Number of identical sections	20
	PP slot opening angle	$\pi/300$ rad
D	Airgap diameter	6.0 m
w_{PP}	Radial thickness of PPs	31.4 mm
	Radial thickness of HS rotor PMs	39.8 mm
	Radial thickness of stator PMs	25.2 mm
	Length of inner airgap	6.0 mm
	Length of outer airgap	6.0 mm
l_a	Active axial length	1.66 m
	HS rotor pole arc to pole pitch ratio	0.8
B_r	Remanence of N48SH PMs at 100°C	1.25 T
μ_r	Relative recoil permeability of PMs	1.05
	Copper packing factor	0.5
	Current density at rated power	2.0 A _{rms} /mm ²
	PM mass	13.5 tons
	HS rotor and PP rotor laminated steel mass	14 tons
	Stator laminated steel mass	15.5 tons
	Copper mass	7 tons
	Estimated structural mass **	100 tons
	Estimated total mass	150 tons

** The structural mass for the 10MW design is assumed to be 2 times the active mass, a similar factor as for the 10MW design given by Magnomatics in [15].

Fig. 9-Fig. 10 compare the analytical and FE predicted radial components of the flux density in the airgaps of the MG element of the PDD. It can be seen, that a very good agreement exists. In addition Fig. 11 compares the transmitted torque and it can be seen a very good agreement exists between the analytical and FE predictions.

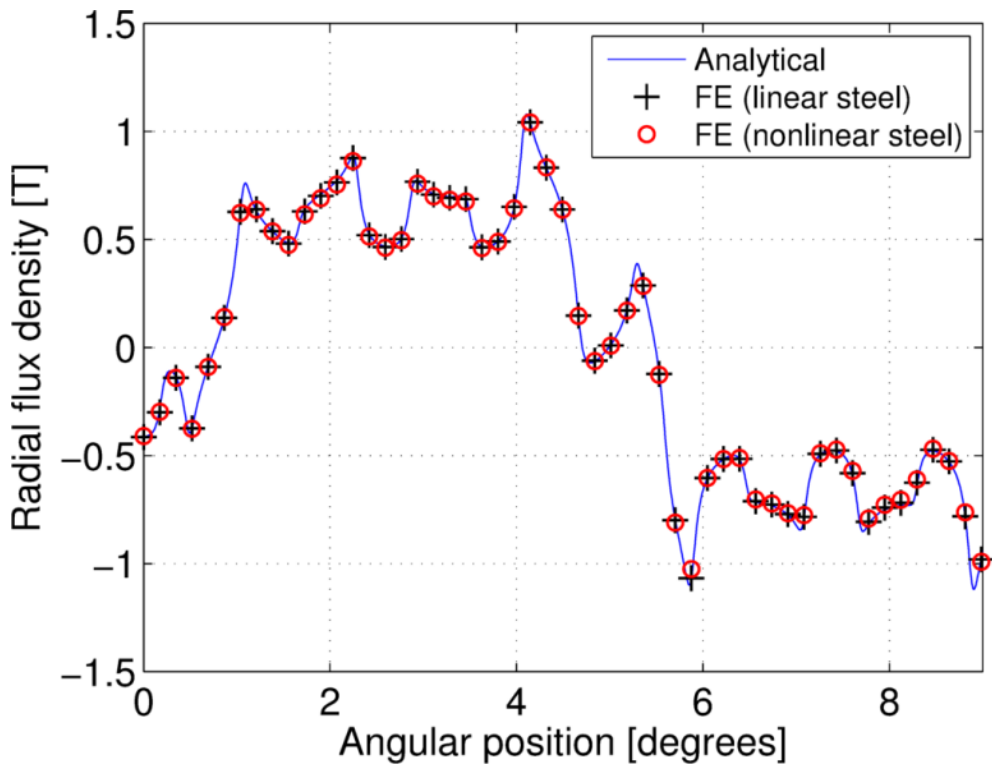


Fig. 9. Radial flux density in the inner airgap.

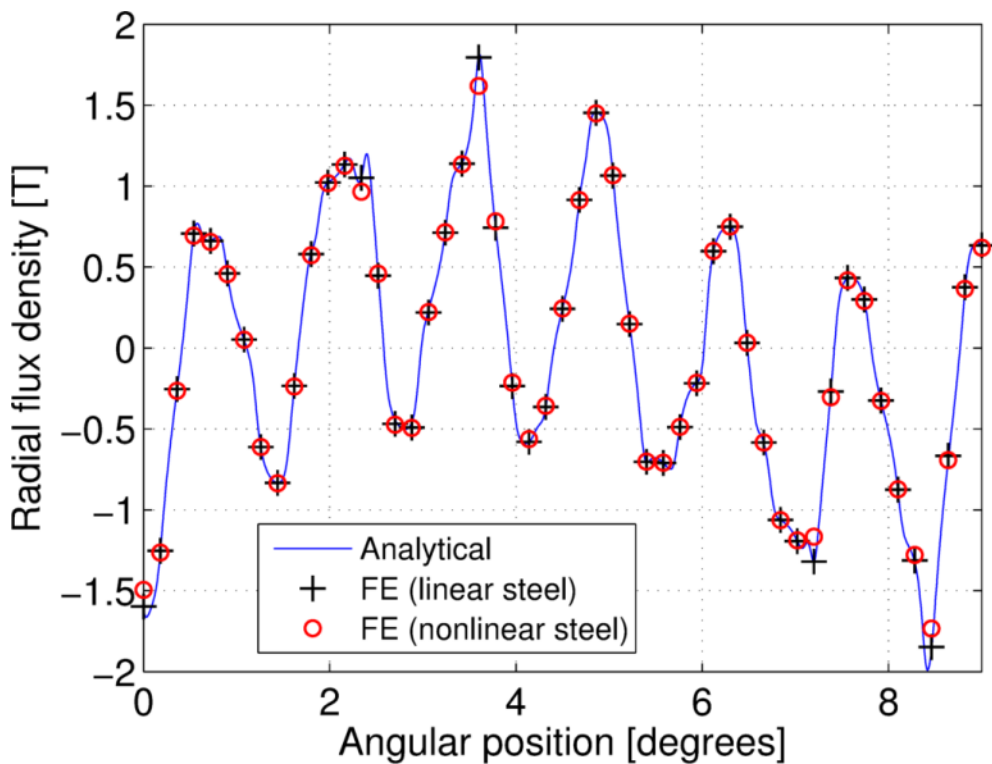


Fig. 10. Radial flux density in the outer airgap.

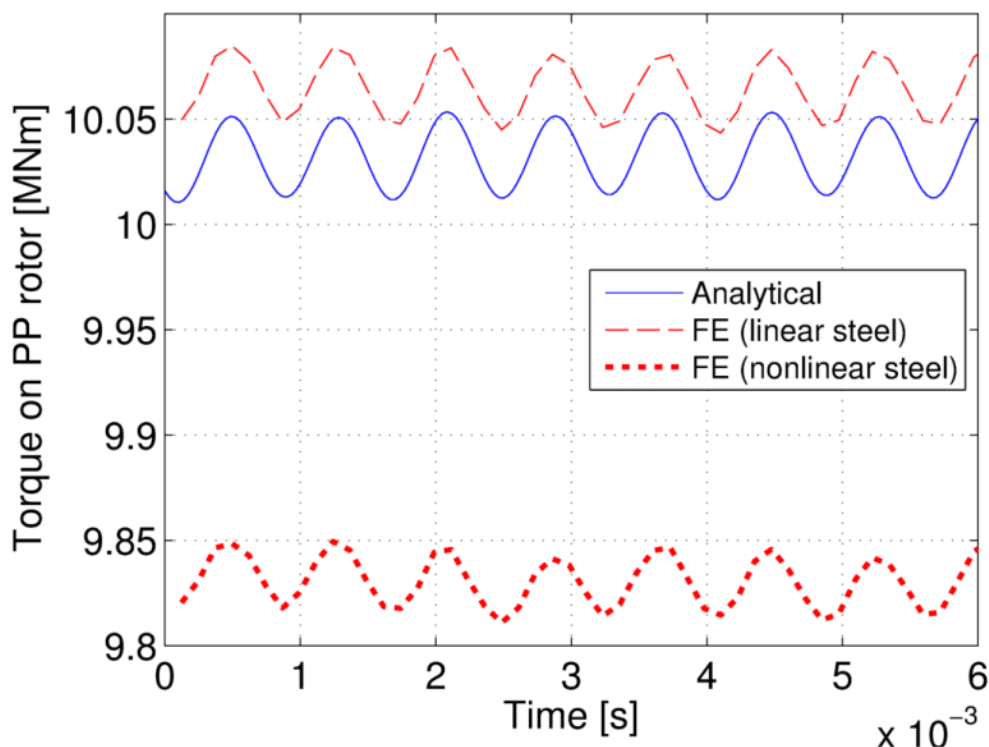


Fig. 11. Variation of transmitted torque on the PP rotor with time.

At the mean radial position of the PP rotor $(R_{PPi} + R_{PPo})/2$, Fig. 12 and Fig. 13 show the variation of the radial and circumferential components of the flux density in a PP with the relative circumferential position on a PP. In addition, at the relative circumferential position $\theta_{PP}/2$ in a PP Fig. 14 and Fig. 15 show the variation of the radial and circumferential components of the flux density in a PP with the relative radial position on the PP. A good agreement exists between FE and analytical predictions. However, although the introduction of the non-linear steel characteristic results in increased discrepancies between the analytical model and FE analysis, this has minimal impact on the prediction of the iron losses in the PPs as can be seen in section 5.

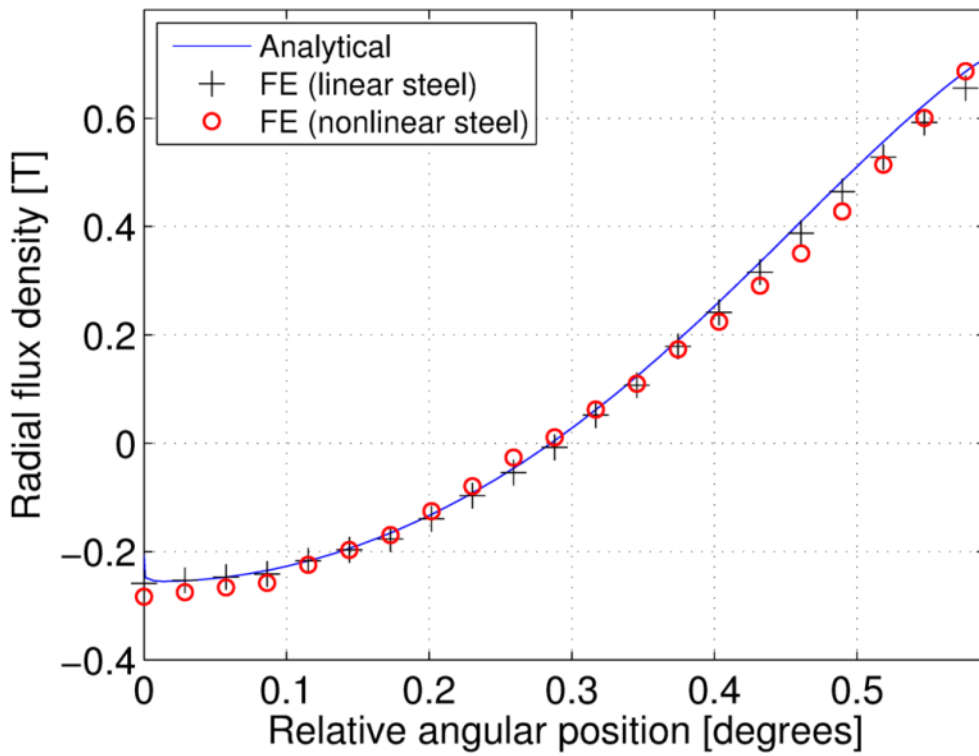


Fig. 12. Variation of radial magnetic flux density in one PP with the relative circumferential position at the mean radial position of the PP.

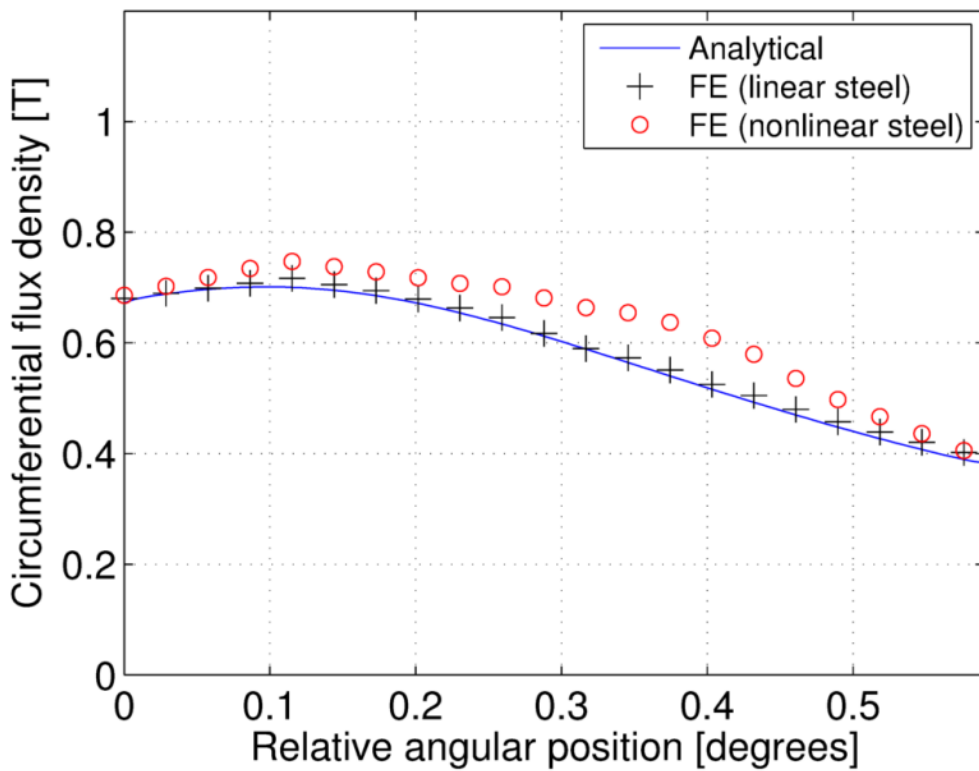


Fig. 13. Variation of circumferential magnetic flux density in one PP with the relative circumferential position at the mean radial position of the PP.

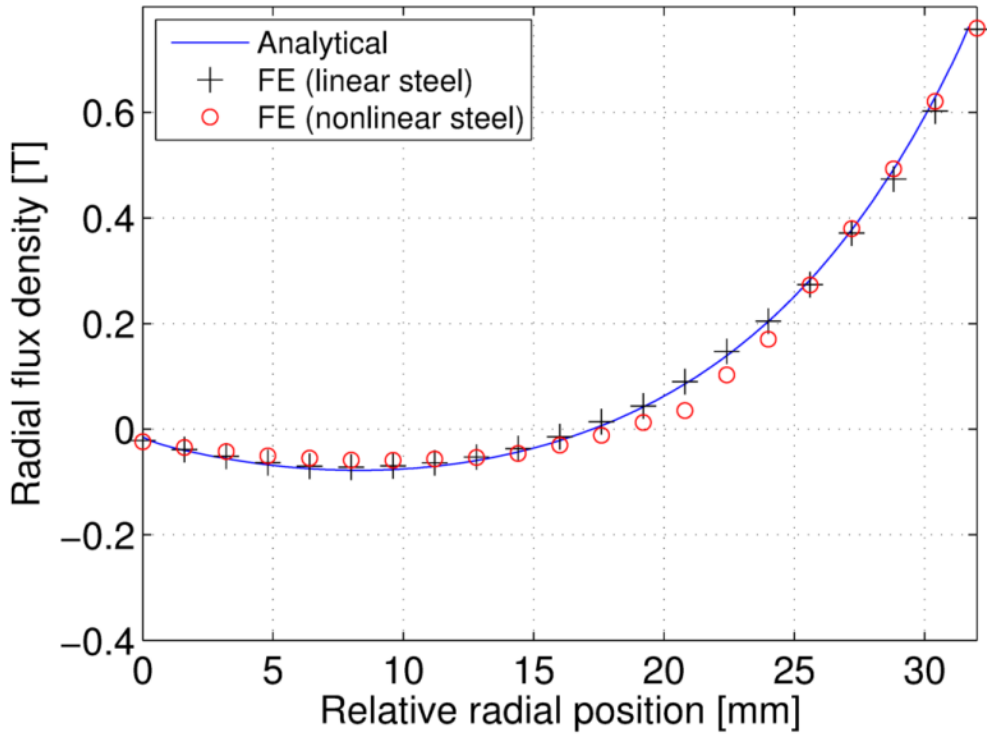


Fig. 14. Variation of radial magnetic flux density in one PP with the relative radial position at the relative circumferential position $\theta_{PP}/2$.

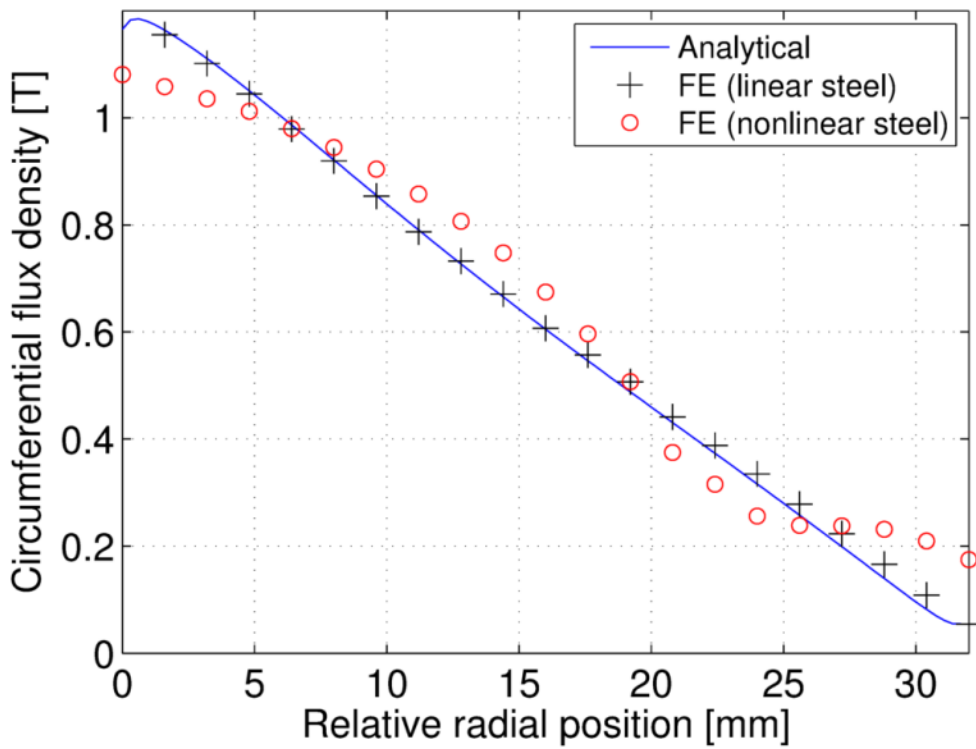


Fig. 15. Variation of circumferential magnetic flux density in one PP with the relative radial position at the relative circumferential position $\theta_{PP}/2$.

Fig. 17 shows the circumferential flux density against the radial flux density distribution at the centre position of one PP for one PP electrical cycle. It may be worth mentioning that the fundamental electrical frequency of the flux density waveforms on the PPs is different from the stator and it is given by:

$$f_{PP,el} = \frac{G - 1}{G} f_{out} \quad (80)$$

where f_{out} is the electrical output frequency of the PDD. It can be seen that at the centre of a PP there is good agreement between the analytical and FE predictions, and the flux density is mainly rotating.

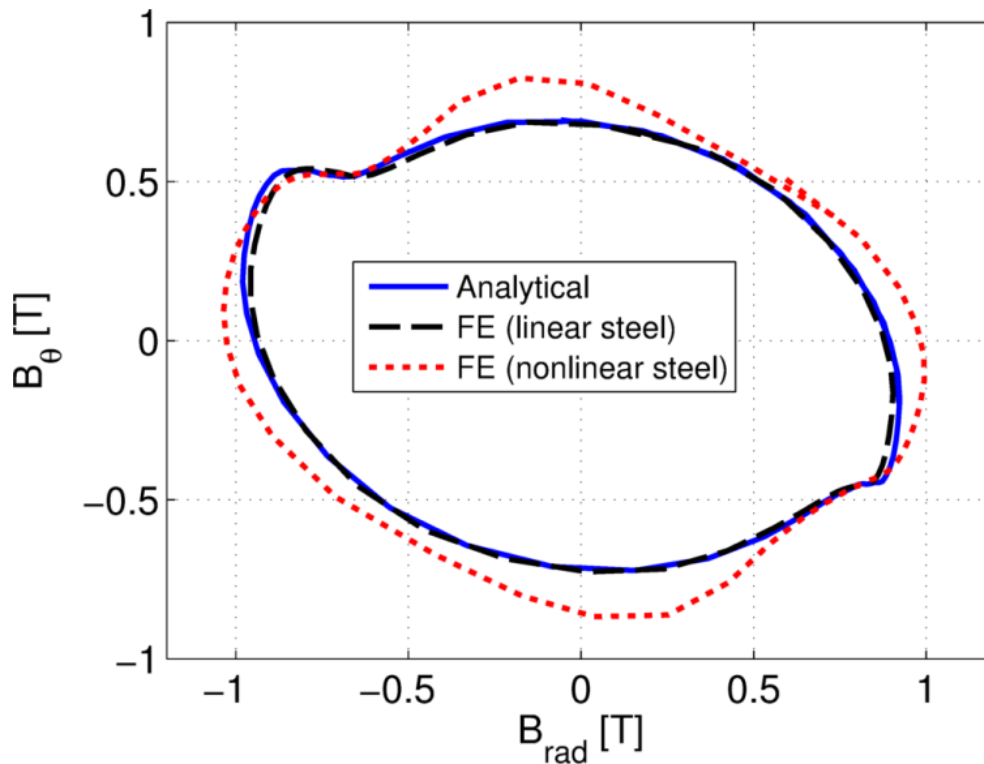


Fig. 16. Variation of circumferential magnetic flux density against radial flux density for one PP electric cycle.

Fig. 17-Fig. 20 show the average flux density distribution at the stator tooth and back-iron for no-load and full-load conditions with time. It can be seen, that a good agreement exists between analytical and FE model.

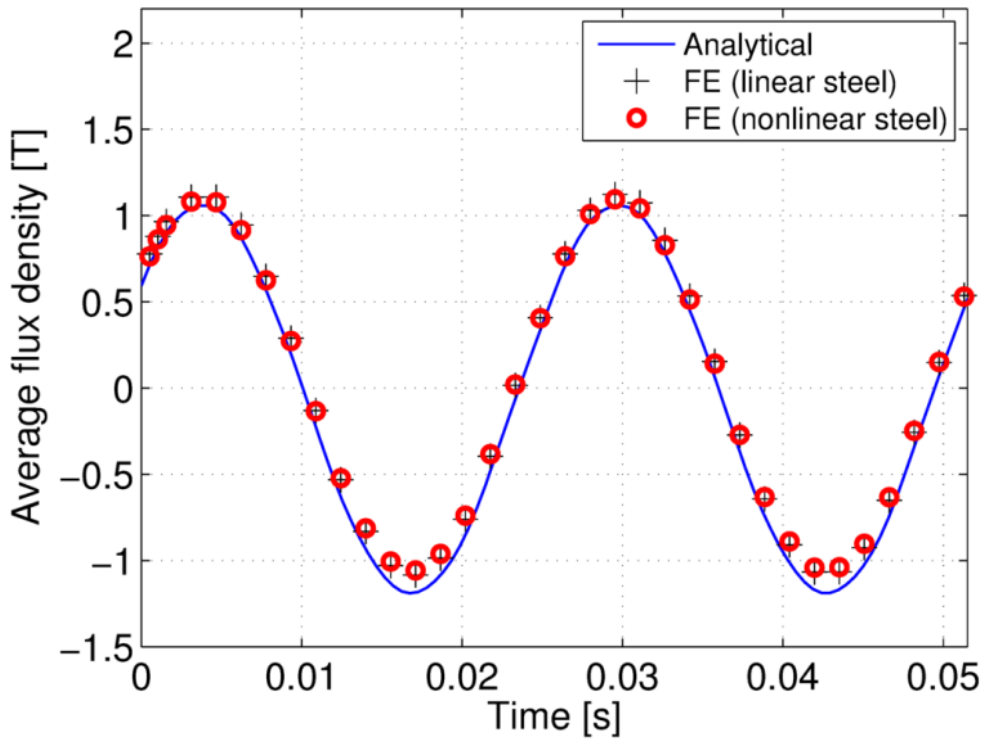


Fig. 17. Variation of average magnetic flux density at the back of one stator tooth with time at rated speed on no-load conditions.

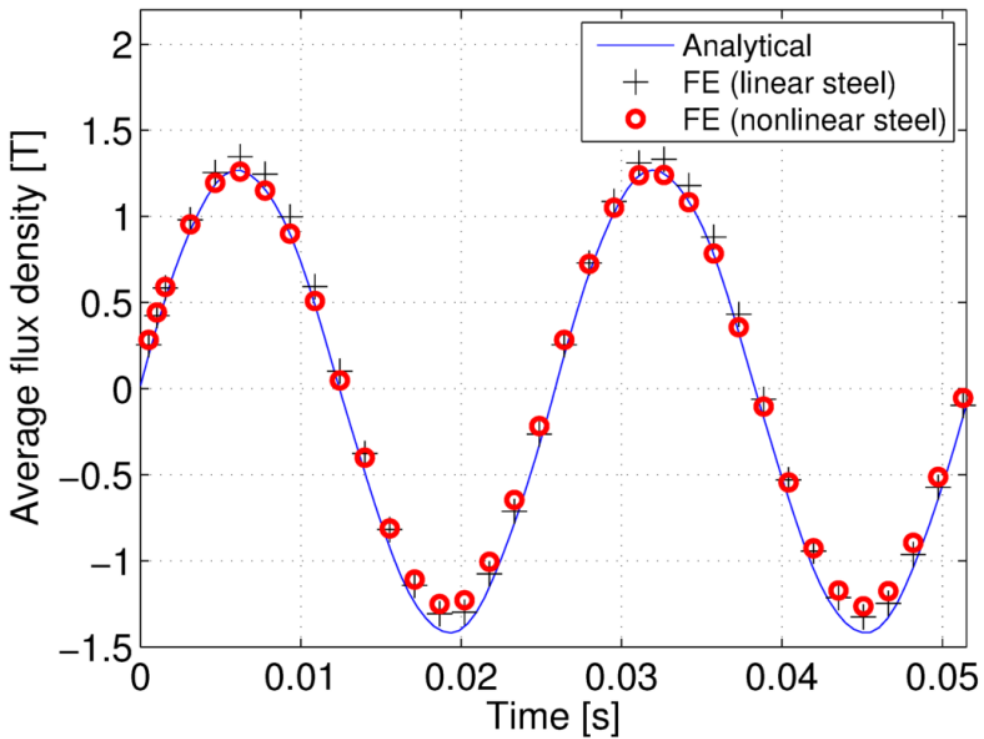


Fig. 18. Variation of average magnetic flux density at the back of one stator tooth with time at rated speed on full-load conditions.

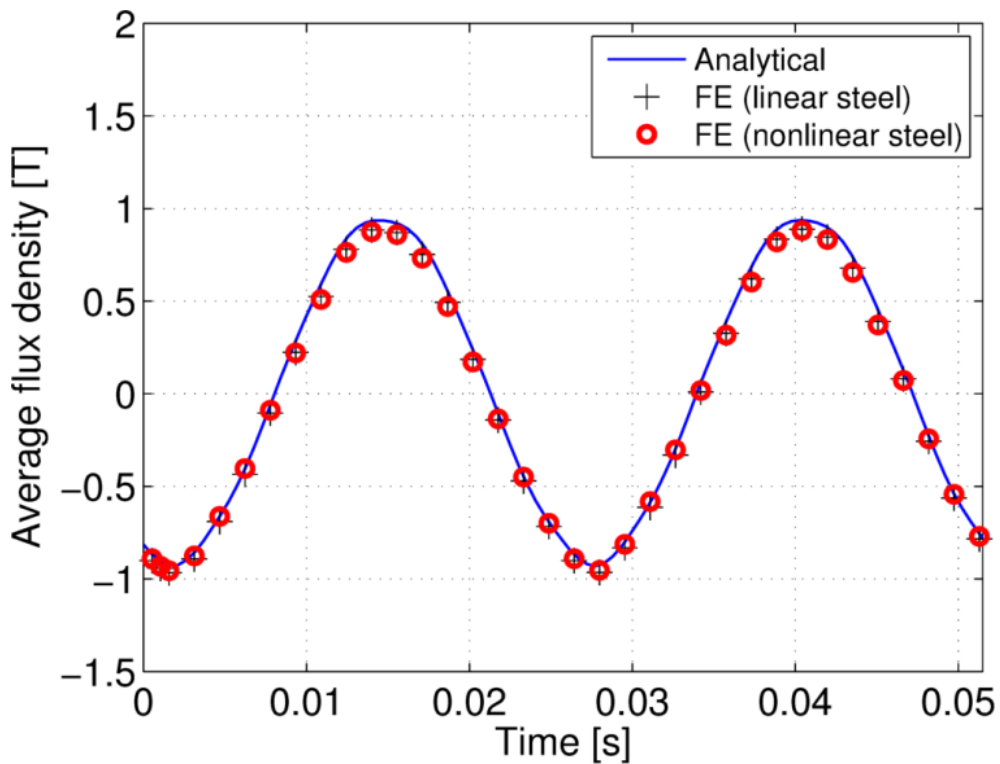


Fig. 19. Variation of average magnetic flux density at the back-iron with time at rated speed on no-load conditions.

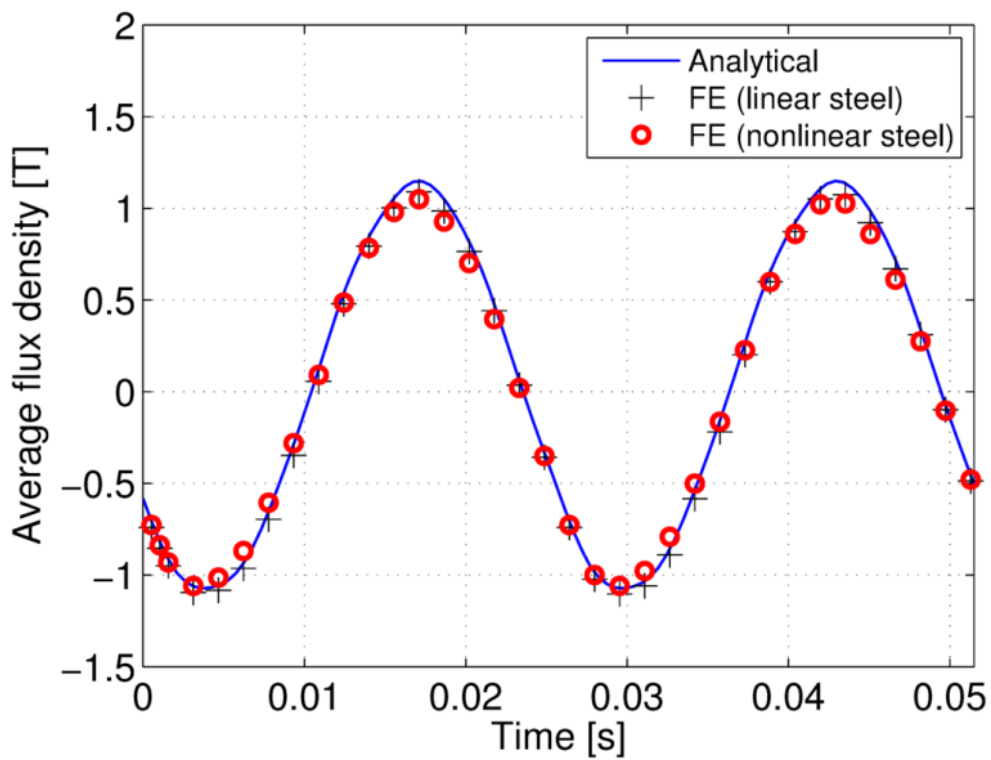


Fig. 20. Variation of average magnetic flux density at the back-iron with time at rated speed on full-load conditions.

5 ELECTROMAGNETIC LOSS ANALYSIS

Two sources of losses have been considered in the analysis: the copper loss and the iron loss. The copper loss is given by

$$P_{Cu} = 2\pi\rho_{Cu}(l_a + l_e)R_S J_{rms} Q_{rms} \quad (81)$$

where l_a and l_e are the active and end winding length, ρ_{Cu} is the resistivity of copper, and J_{rms} is the rms current density in the windings. The electric loading is given by [10]:

$$Q_{rms} = \frac{\sqrt{2}}{2\pi} \frac{1}{k_w R_S^2 l_a B_{p,S}} \frac{P_{AC}}{\Omega_{PP} G} \quad (82)$$

where k_w is the winding factor, $B_{p,S}$ is the peak fundamental flux density at the stator bore radius R_S , Ω_{PP} is the rotational speed of the PP rotor, G is the gear ratio and P_{AC} is the power. The iron loss is calculated by adding the various loss components [11]:

$$P_{iron} = P_{hyst} + P_{class} + P_{exc} \quad (83)$$

where P_{hyst} is the hysteresis loss, P_{class} is the classical eddy current loss and P_{exc} is the excess eddy current loss. The hysteresis loss is given by

$$P_{hyst} = k_{hyst} f B_m^\alpha \left(1 + \frac{0.65}{B_m} \sum_{i=1}^{N_{ml}} \Delta B_i \right) \quad (84)$$

where f is the frequency of the flux density waveform, k_h and α are constants, N_{ml} the number of minor loops and ΔB_i is the change in flux density during the excursion around a minor loop. Since the flux density in the stator iron may be offset due to the PMs on the stator it is assumed that the hysteresis loss is only dependent on the relative deviation of the flux density. Therefore, only the amplitude of the major loop

$$B_m = (B_{max} - B_{min})/2 \quad (85)$$

is considered, where B_{max} and B_{min} are the maximum and minimum flux density. The classical eddy current loss is given by

$$P_{class} = \frac{\sigma_L d^2}{12m_L} f \int_0^{1/f} \left(\frac{dB}{dt} \right)^2 dt \quad (86)$$

where σ_L is the electrical conductivity, m_L is the lamination mass density and d the lamination thickness. The excess eddy current loss is given by

$$P_{exc} = k_{exc} f \int_0^{1/f} \left| \frac{dB}{dt} \right|^{1.5} dt \quad (87)$$

For rotational flux density conditions, the iron loss is approximated by adding the iron loss associated with the radial and circumferential flux density waveforms. The mechanical losses, the AC losses in the windings and the eddy current losses in the PMs are neglected in the analysis. The parameters for the loss calculation are given in Table III.

TABLE III
Parameters For the Loss Calculation

Symbol	Quantity	Value
k_{hyst}	Hysteresis coefficient	17.9×10^{-3}
α	Hysteresis exponent	2.0
k_{exc}	Excess loss coefficient	$0.2 \times 10^{-3} \text{ W s}^{1.5} \text{ T}^{-1.5} \text{ kg}^{-1}$
d	Lamination thickness	0.35 mm
m_L	Mass density of laminations	$7.61 \times 10^3 \text{ kg m}^{-3}$
σ_L	Conductivity	$2.22 \times 10^6 \text{ } \Omega^{-1} \text{ m}^{-1}$
m_{Cu}	Mass density of copper	$8.96 \times 10^3 \text{ kg m}^{-3}$
ρ_{Cu}	Resistivity of copper at 120°C	$2.4 \times 10^{-8} \text{ } \Omega \text{ m}$

Fig. 21 shows the variation of losses with output power for the PDD in Table II, where it can be seen that good agreement between the analytical and FE exists. For the loss calculation at partial load it is assumed, that at wind speeds below the rated wind speed the rotor speed is kept proportional to the wind speed to achieve a maximum energy yield [12]. Fig. 22 shows the variation of efficiency with output power. It can be seen, that efficiencies in excess of 98.5% can be achieved.

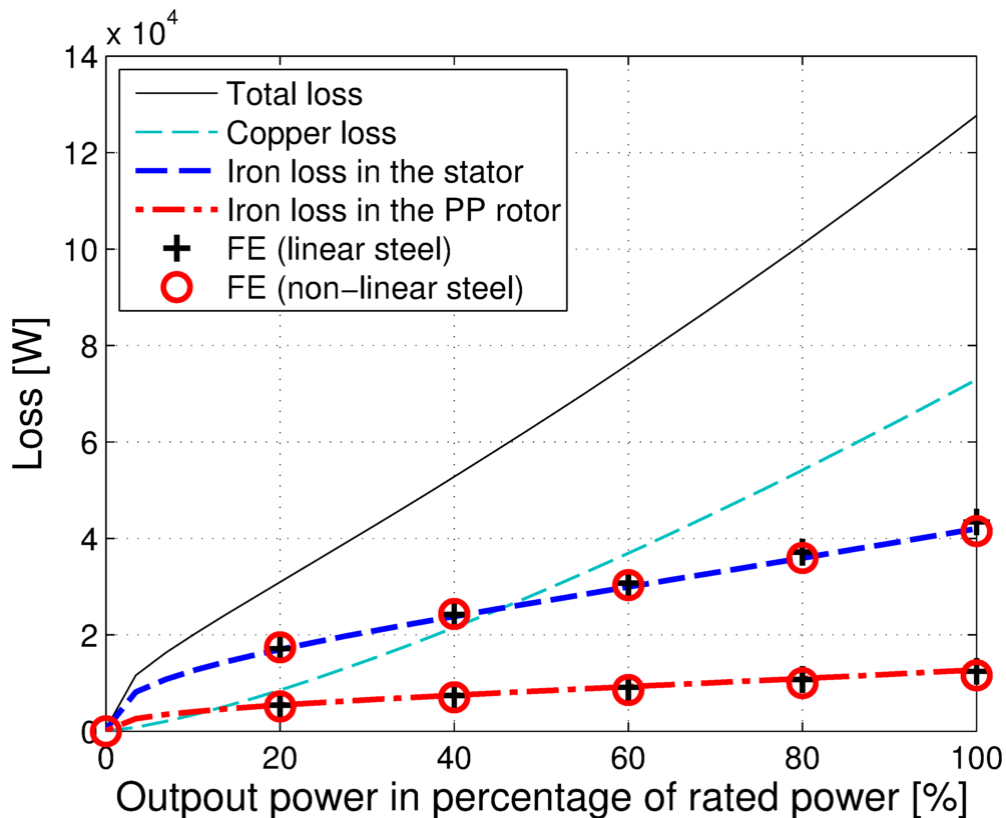


Fig. 21. Variation of losses with the output power for the PDD in Table II.

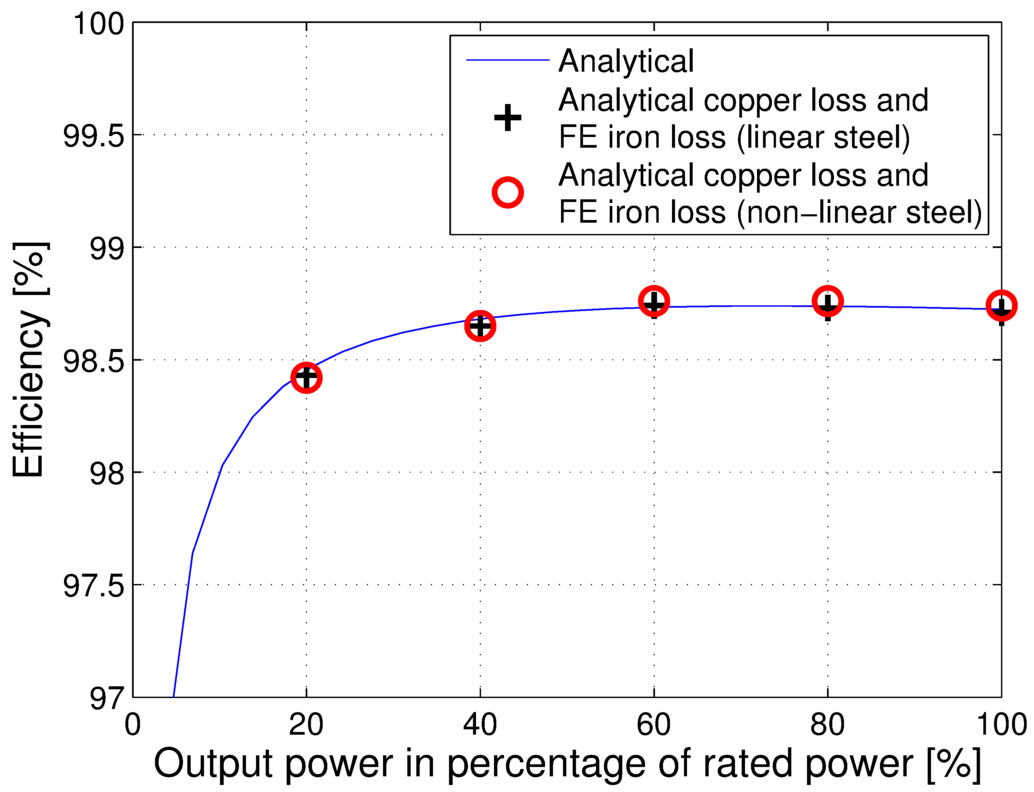


Fig. 22. Variation of efficiency with the output power for the PDD in Table II.

6 DESIGN AND OPTIMISATION PROCEDURE

The analytical models developed in chapters 2 and 5 are employed to calculate main design parameters of the PDD, such as the shear stress in the MG element of the PDD and the efficiency. The optimisation has been performed by employing the developed models according to the flowchart in Fig. 23. The procedure has been implemented into MATLAB code, while the parameters for the MG and the PDD are supplied by a pre-selected parameter set in text file format. The output is supplied both in form of MATLAB MAT-file objects and in form of graphical output as MATLAB FIG-files. The output may readily be converted through MATLAB into other common formats. Furthermore, the code can be exported into other common languages, such as C++, and can be combined with a graphical user interface (GUI).

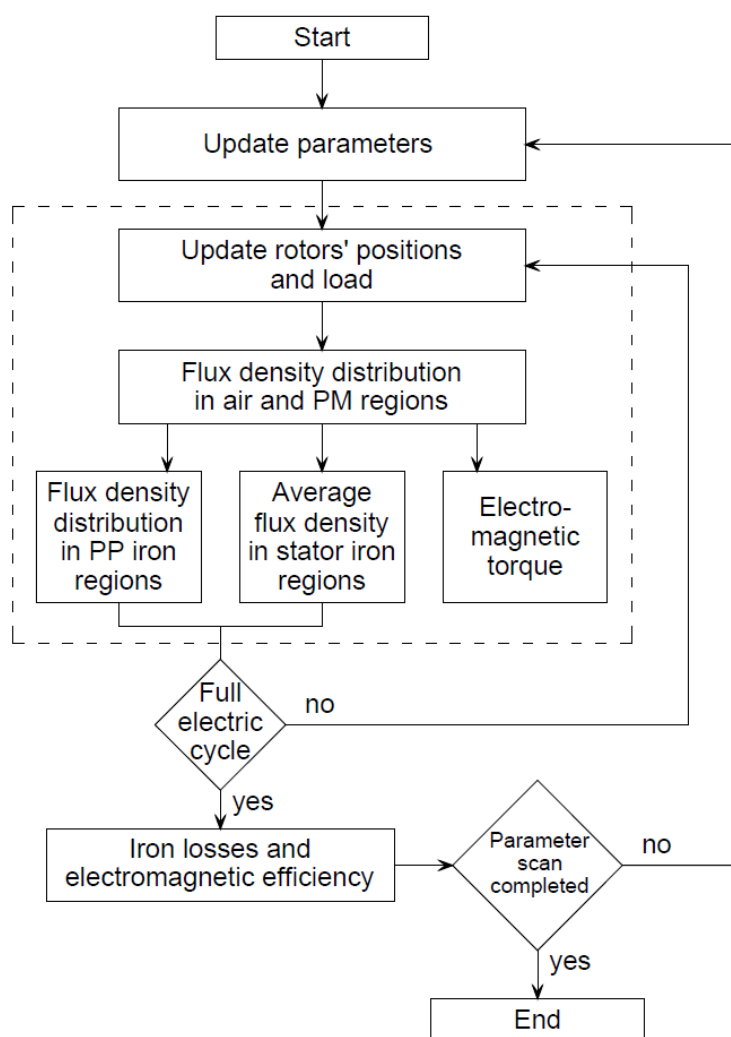


Fig. 23. Flowchart for the analytical model and the optimisation.

6.1 Optimisation of the Magnetic Gear component for a 10MW wind turbine

The MG element of the PDD has been optimised to achieve the maximum achievable equivalent shear stress with the minimum PM mass. The equivalent shear stress is given by [7]:

$$\sigma = \frac{2T_{PP}}{\pi D^2 l_a} \quad (88)$$

where D is the airgap diameter and T_{PP} is the torque on the PP rotor. Fig. 24 shows the variation of the required PM mass with the achievable equivalent shear stress for radial magnetisation (RM), continuous HM (cHM), and discrete HM (dHM, four segments per pole pair) on either HS rotor or stator, for a MG with the same pole-numbers, PP radial and circumferential dimensions, and airgap lengths as the MG component given in Table II. It can be seen that adopting a cHM on both HS rotor and stator results in the highest shear stress for a given PM mass. However, in practice, the realization of a cHM is difficult, although it could be better approximated by employing a discrete HM with a larger number of segments per pole-pair. Furthermore, it can be seen, that using a discrete HM with a low number of segmentation (4 segments per pole pair) on the stator would also result in a significant improvement of the shear stress. Replacing the RM PMs on the HS rotor by a discrete HM (four segments per pole-pair) also results in designs with higher shear stress, albeit, the benefits are only apparent for larger PM masses (more than 17 tons), while for a smaller shear stress the required PM mass may be significantly increased. Therefore, for the designs with a smaller shear stress, a RM on the HS rotor may be more desirable than a dHM in terms of PM mass reduction.

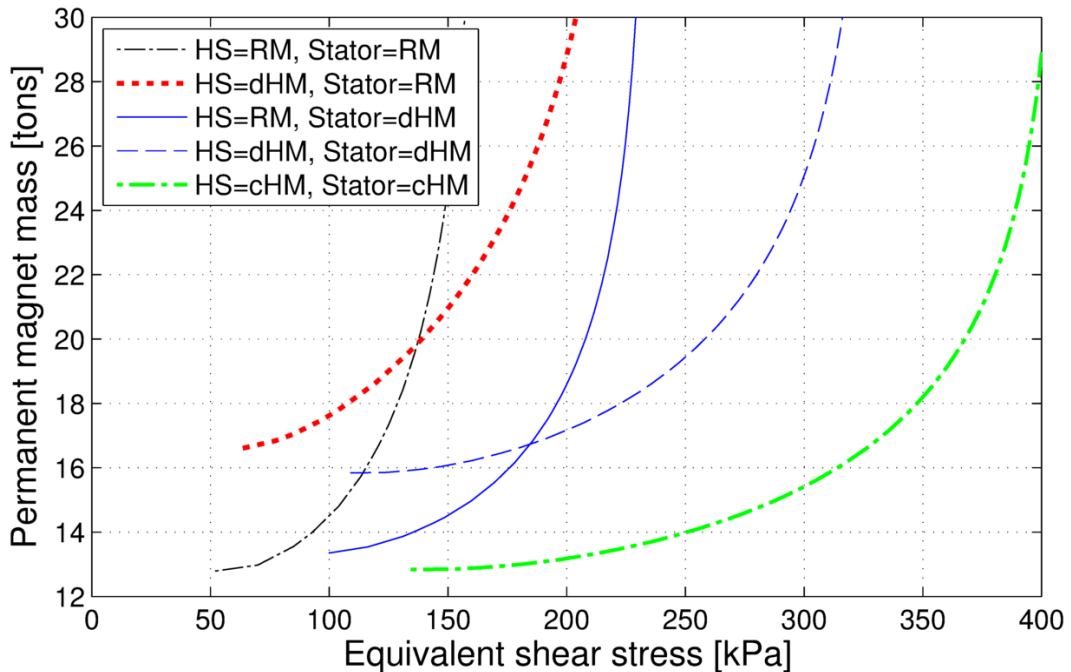


Fig. 24. Variation of the PM mass with the achievable equivalent shear stress, with either radial magnetisation (RM), continuous Halbach magnetisation (cHM) or discrete Halbach magnetisation (dHM) on HS rotor and stator.

The mass of the laminated steel for the HS rotor and stator back-iron, and the PP rotor is calculated for each data point. The required radial width of the back-iron for the HS rotor is estimated as

$$w_{HS,iron} = \frac{R_{HS} B_{pHS}(R_{HS})}{p_{HS} B_{sat}} + \frac{R_{HS} B_{pS}(R_{HS})}{p_S B_{sat}} \quad (89)$$

where $B_{p_{HS}}(R_{HS})$ and $B_{p_S}(R_{HS})$ are the peak fundamental flux density at the radius R_{HS} , and $B_{sat} = 1.5$ Tesla. Although the stator back-iron of the MG element would be replaced when integrating the MG within a PDD, it may give an indication on the required back-iron. The required radial width of the back-iron for the stator of a MG is estimated as

$$w_{S,iron} = \frac{R_S}{p_{HS}} \frac{B_{p_{HS}}(R_S)}{B_{sat}} + \frac{R_{HS}}{p_S} \frac{B_{p_S}(R_S)}{B_{sat}} \quad (90)$$

where $B_{p_{HS}}(R_S)$ and $B_{p_S}(R_S)$ are the peak fundamental flux density at the radius R_S . Fig. 25 shows the variation of the total active mass of a MG, which includes the PM mass, and the laminated steel of the PP rotor, the HS rotor and the stator back-iron for a MG, with the maximum equivalent shear stress. It can be seen that a shear stress for which the active mass is minimum exists. It can also be seen, that employing a HM, results in significant reductions in the active mass.

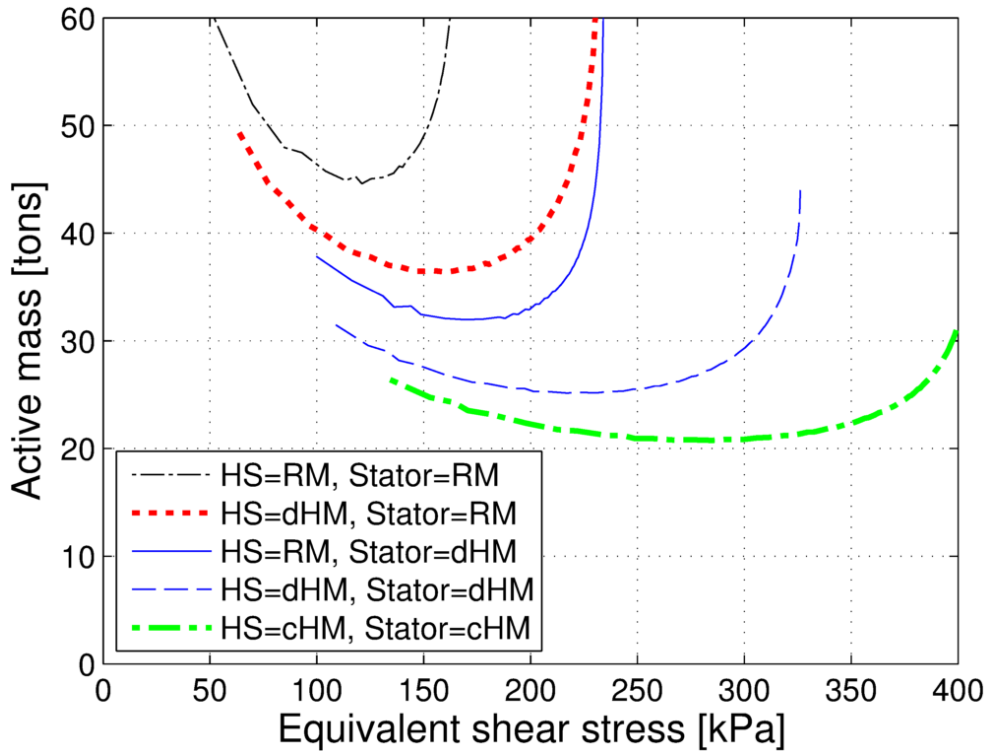


Fig. 25. Variation of the total active mass of a MG with the achievable equivalent shear stress, with either radial magnetisation (RM), continuous Halbach magnetisation (cHM) or discrete Halbach magnetisation (dHM) on HS rotor and stator.

The required PM mass may be further reduced by considering a pole-arc to pole-pitch ratio $\alpha < 1$. Fig. 26 shows the variation of the PM mass with the equivalent shear stress for several α . It can be seen, that $\alpha = 0.8$ achieves a good result for a large range of the equivalent shear stress.

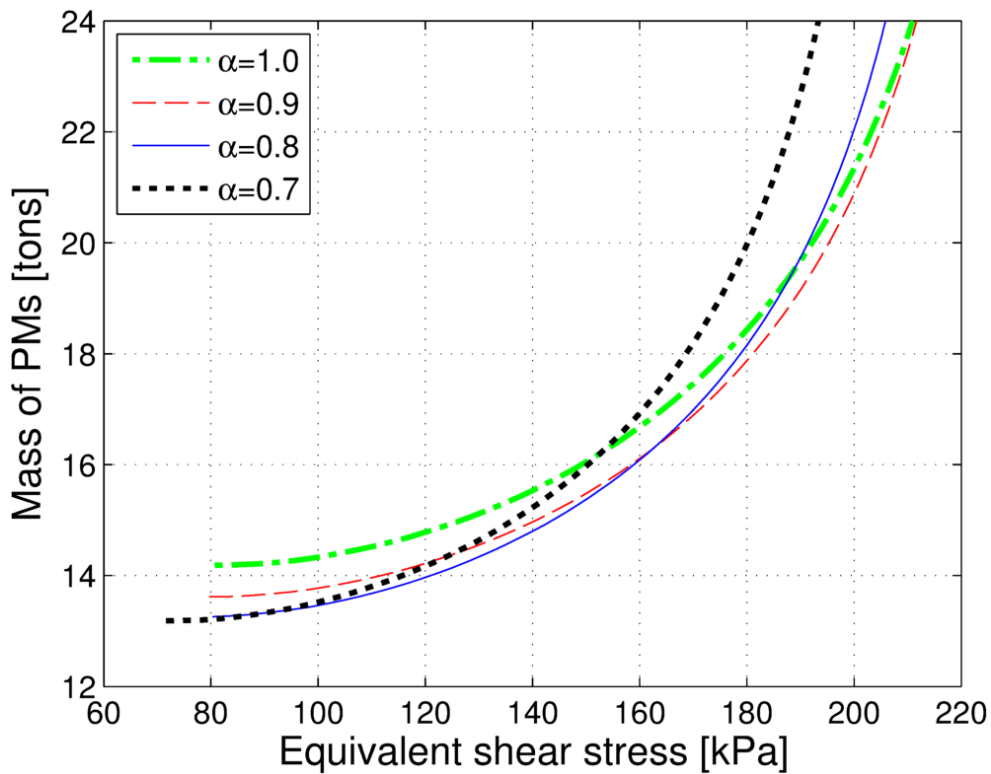


Fig. 26. Variation of the PM mass with the achievable equivalent shear stress for several pole-arc to pole-pitch ratios α .

Fig. 27 shows the variation of the radial peak flux density of the harmonic corresponding to the pole-pair number of the PMs on the HS rotor at the radii at the interfaces between the PMs and the back irons of the laminated steel with the equivalent shear stress. It can be seen, that the peak flux density at R_s decreases significantly for larger values of the shear stress. However, it can also be seen, that the peak flux density remains fairly constant over a large range of the equivalent shear stress, which would make these designs suitable for the integration within a PDD.

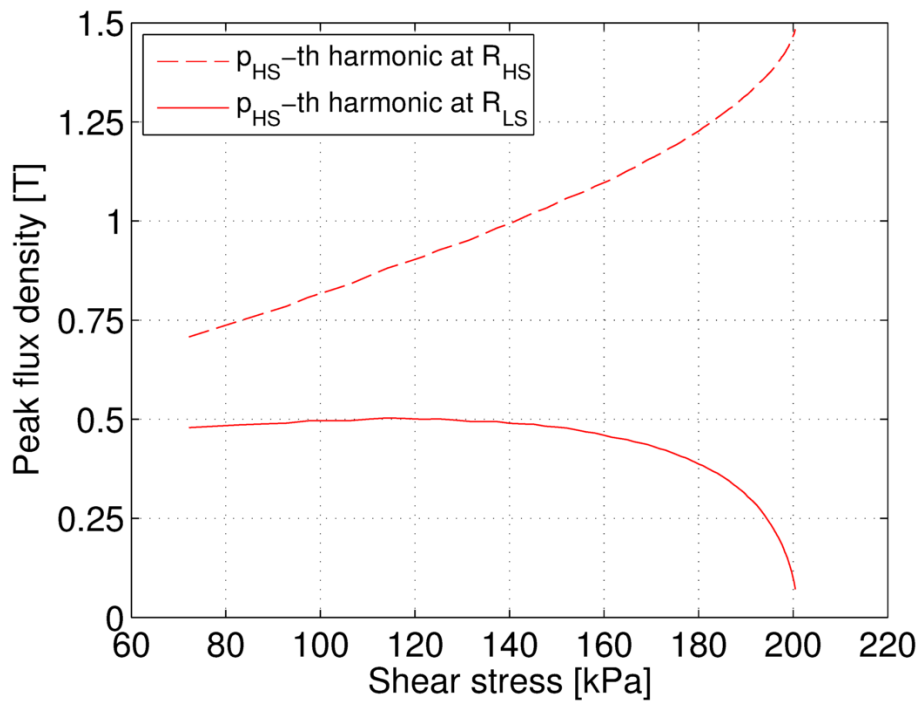


Fig. 27. Variation of radial peak flux density of the harmonic corresponding to the pole-pair number of the PMs on the HS rotor at the radii at the interfaces between the PMs and the back irons.

Fig. 28 shows the variation of the laminated steel required for the HS rotor and PP rotor for $\alpha = 0.8$. It can be seen, that the laminated steel mass reduces with the shear stress. However, this may not be true for the HS rotor, due to the increasingly large flux in the HS rotor steel, see Fig. 27.

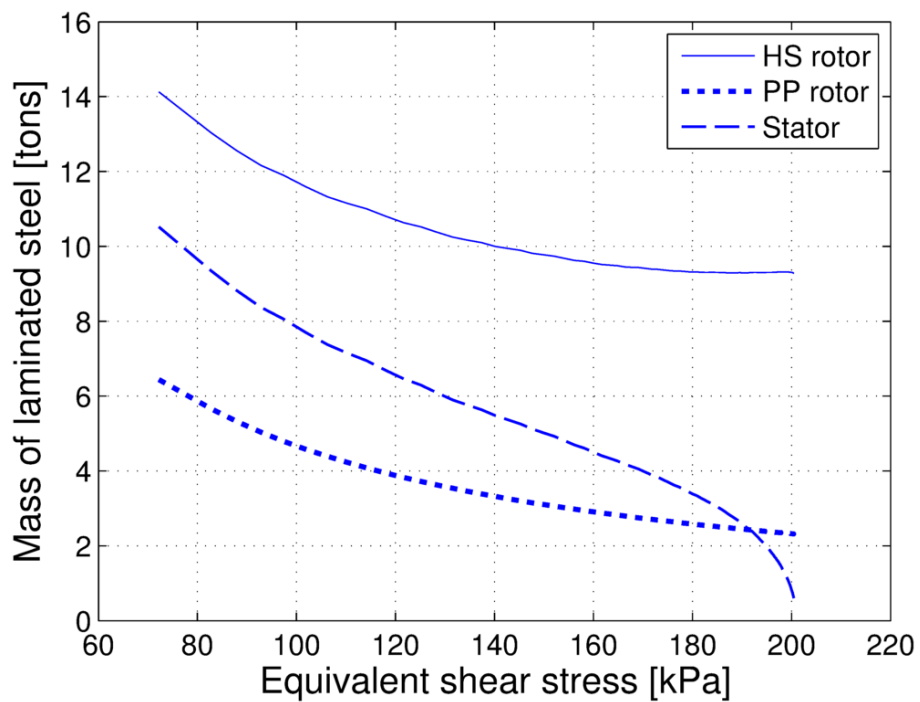


Fig. 28. Variation of laminated steel mass with the equivalent shear stress.

Fig. 29 shows the variation of the equivalent shear stress with the radial PP thickness w_{PP} . It can be seen, that a maximum exists and that the shear stress drops significantly towards small values of w_{PP} . In addition, saturation effects would also significantly reduce the torque transmission capability for small values of w_{PP} , as can also be seen in Fig. 29. Therefore, for the forthcoming analysis the radial PP thickness is selected as

$$w_{PP} = \frac{\pi R_{PP} k}{Q} \quad (91)$$

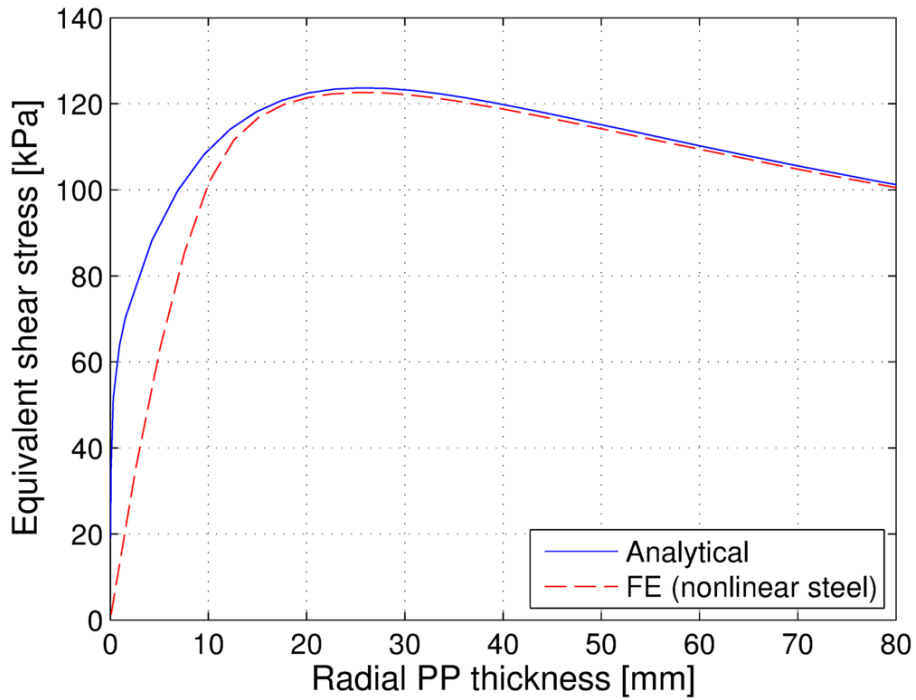


Fig. 29. Variation of equivalent shear stress with the radial PP thickness w_{PP} for the analytical model and for FE with steel with nonlinear characteristics.

Due to the large size of the PDD it might be built from S circumferentially identical sections. It may be worth mentioning at this point, that the rated electrical output frequency supplied by the HS rotor PMs of the MG component is then given by

$$f_{out,R} = G \Omega_{PP,R} S p_{HS}^* \quad (92)$$

where G is the gear ratio, $\Omega_{PP,R}$ is the rated speed of the PP rotor, and p_{HS}^* is the number of pole-pairs per section on the HS rotor. Fig. 30 and Fig. 31 show the variation of the PM mass in the MG element of the PDD with the achievable equivalent shear stress for several numbers of symmetrical sections S and if the gear ratio is $G = 7.5$. The sections have the same number of poles on HS rotor and stator as the MG element in Table II. It can be seen, that for a given equivalent shear stress a number of sections exist, for which the PM mass is minimum.

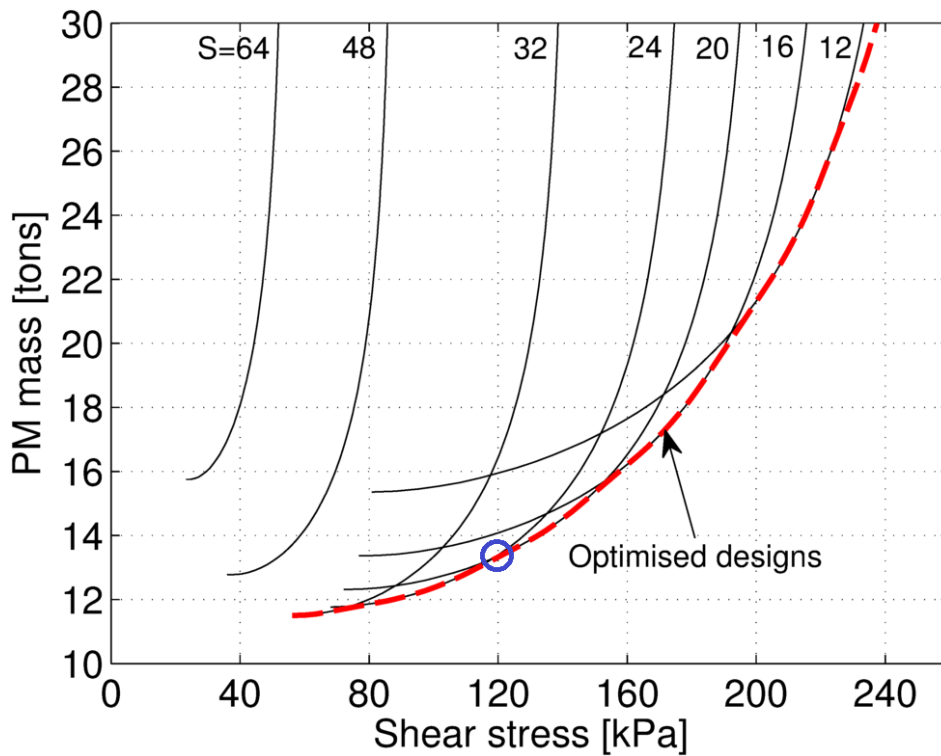


Fig. 30. Variation of the PM mass with the achievable equivalent shear stress, where the number of PM pole-pairs and PPs per section are the same as for the MG in Table II, for several numbers of symmetrical sections S.

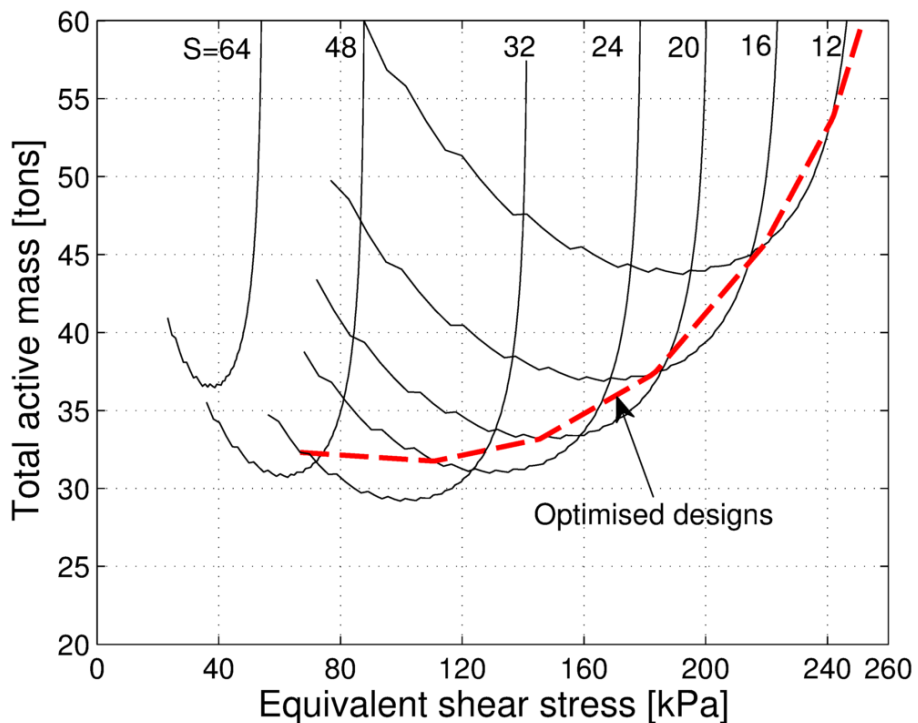


Fig. 31. Variation of total active mass for MGs with the achievable equivalent shear stress, where the number of PM pole-pairs and PPs per section are the same as for the MG in Table II, for several numbers of magnetically identical sections S.

Furthermore, Fig. 32 and Fig. 33 show the variation of the PM mass and the total active mass for a MG with the achievable equivalent shear stress for several gear ratios G if all numbers of symmetrical sections S are considered (Optimised designs). It can be seen, that at lower equivalent shear stresses and for the shown gear ratios the PM mass and total active mass is lower for smaller gear ratios. Finally, the design for the MG element given in Table II has been highlighted in Fig. 30 and Fig. 32.

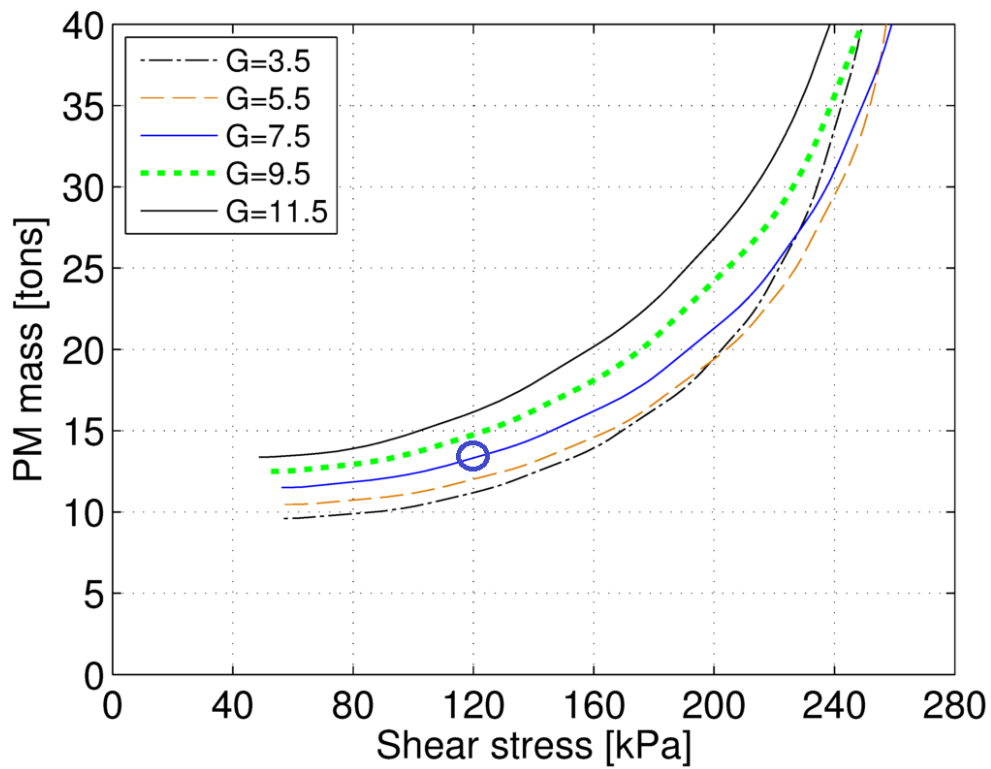


Fig. 32. Variation of the PM mass with the achievable equivalent shear stress for several gear ratios G , if all possible numbers of symmetrical sections are considered.

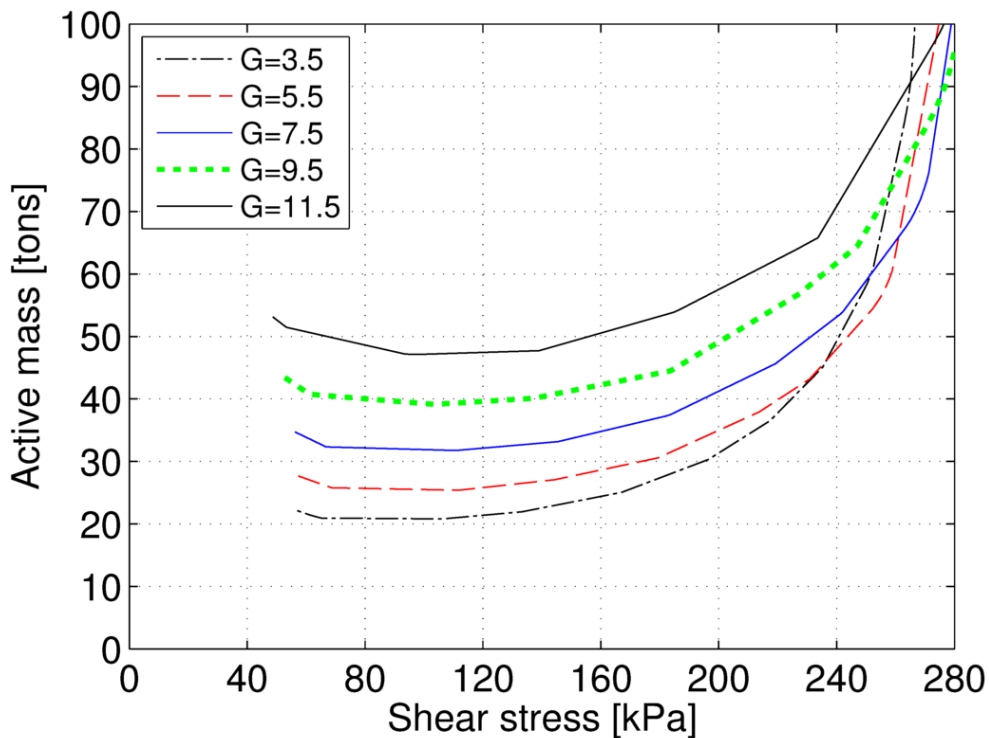


Fig. 33. Variation of the total active mass of a MG with the achievable equivalent shear stress for several gear ratios G , if all possible numbers of symmetrical sections are considered.

In general the aspect ratio of the MG element of the PDD may have a significant effect on the performance and the active masses of the PDD. Fig. 34, therefore, shows the variation of the achievable equivalent shear stress with the airgap diameter, when the dimensions of the PPs and the PMs are varied linearly with the airgap diameter (and where the design for the MG element is the benchmark design in Table II). It can be seen, that the equivalent shear stress depends significantly on the airgap diameter. It can also be seen, that if the airgap length is selected as a fixed percentage of the airgap diameter (here 0.1%), the achievable equivalent shear stress is constant and independent of the airgap diameter. Furthermore, due to the constant equivalent shear stress also the PM mass, and the HS rotor and PP rotor laminated steel mass would remain constant.

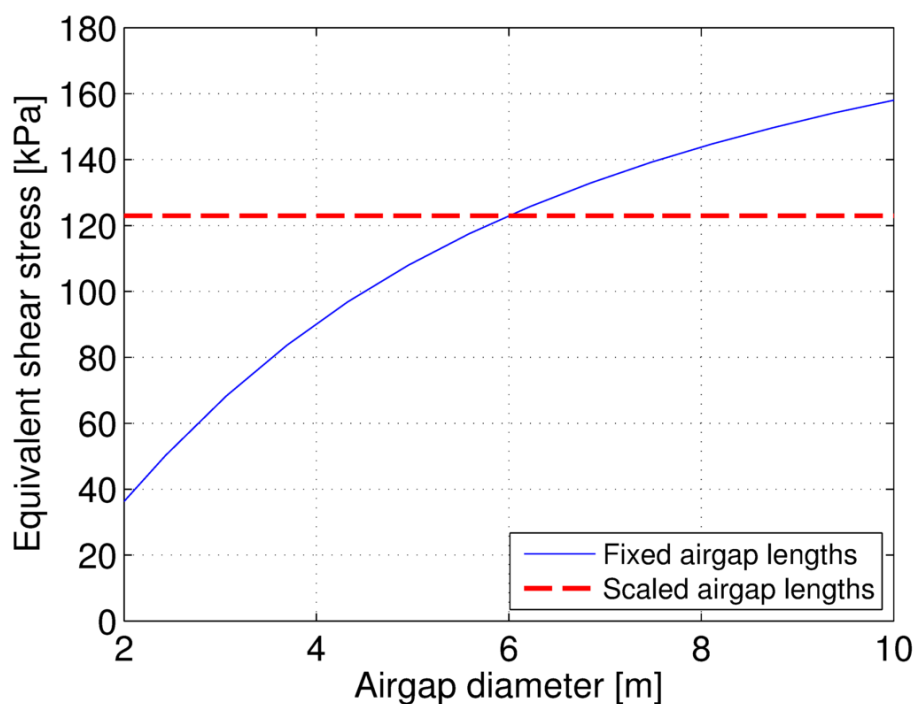


Fig. 34. Variation of equivalent shear stress for the selected MG component with the airgap diameter for fixed and scaled airgaps. The PM and PP dimensions are scaled with the airgap diameter.

6.2 Optimisation of the Pseudo-Direct Drive for a 10MW wind turbine

Fig. 35-Fig. 36 show the variation of the copper mass and the stator laminated steel mass with the selected airgap diameter and the current density at rated power. The airgap lengths are scaled linearly with the airgap diameter and the PM mass, and the HS rotor and PP rotor laminated steel mass are therefore given by Table II. It can be seen, that the copper and laminated steel mass decreases for a given current density, when the airgap diameter is increased. Fig. 37 shows the variation of the efficiency with the airgap diameter and the selected current density at rated power. It can be seen, that for a given efficiency a minimum diameter exists. It can also be seen, that for a given current density, increasing the diameter would also increase the efficiency. However, although increasing the diameter would improve the efficiency and decrease the active masses, it could also lead to an increase in the mass of the structural components and the total cost of the PDD [12],[13]. Fig. 38 shows the variation of the efficiency at rated power with the active mass. It can be seen, that efficiencies in excess of 99.0% may be achieved. It can also be seen, that a PDD with an efficiency of 98.0% can be achieved with an active mass of about 45tons.

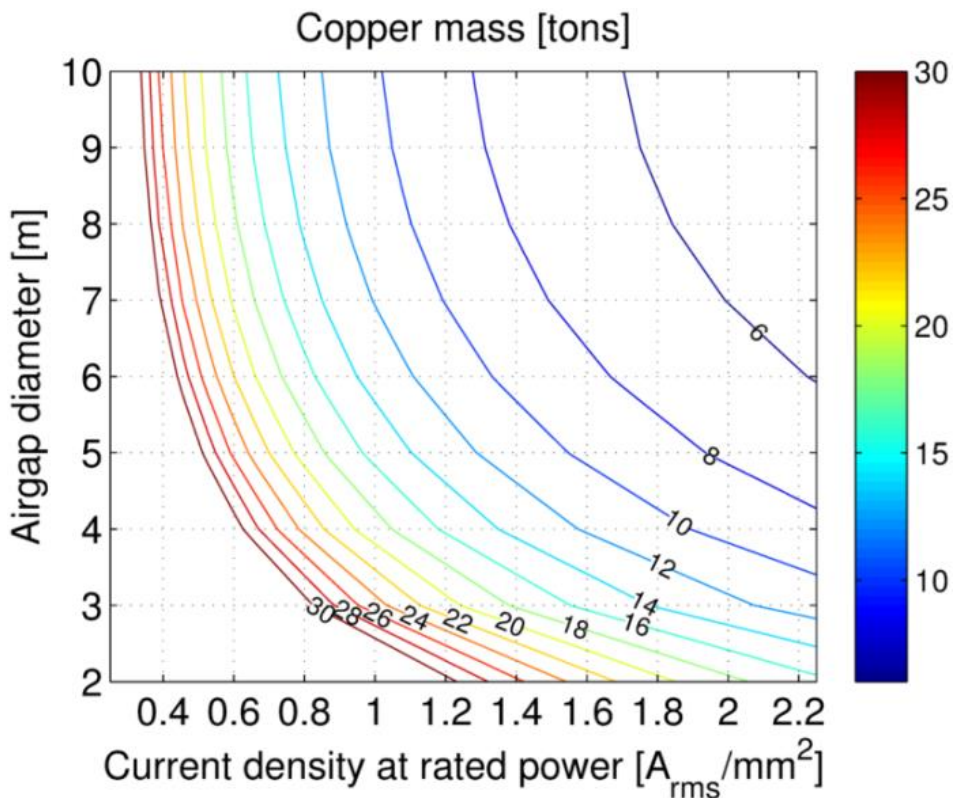


Fig. 35. Variation of copper mass with the airgap diameter and the current density at rated power.

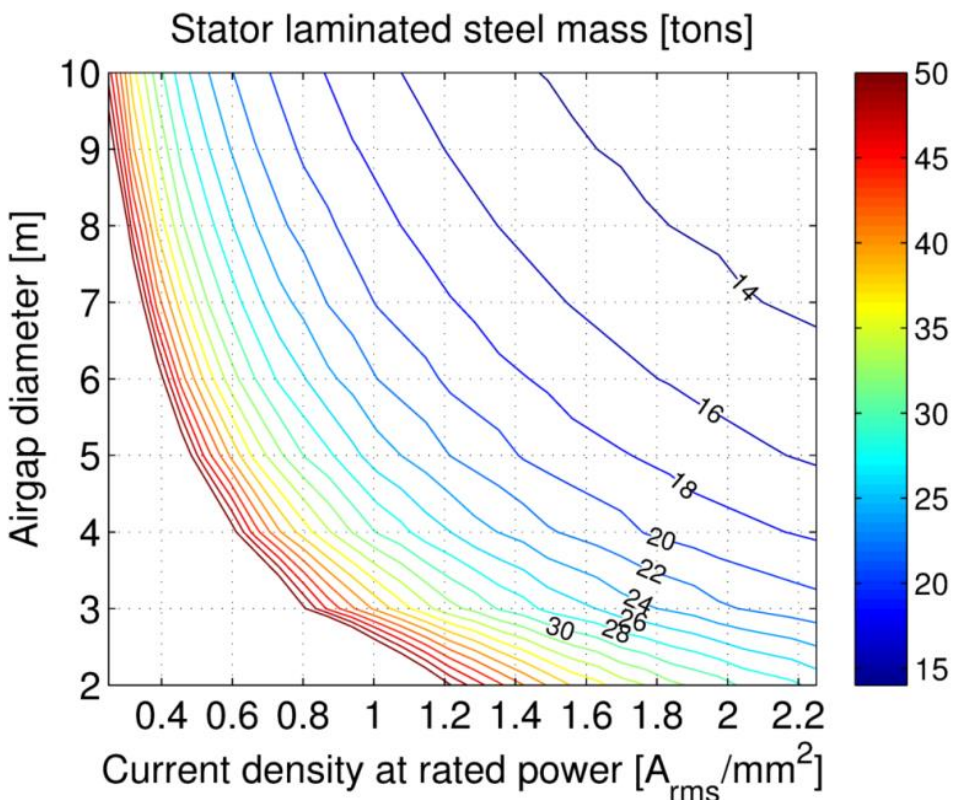


Fig. 36. Variation of stator laminated steel mass with the airgap diameter and the current density at rated power.

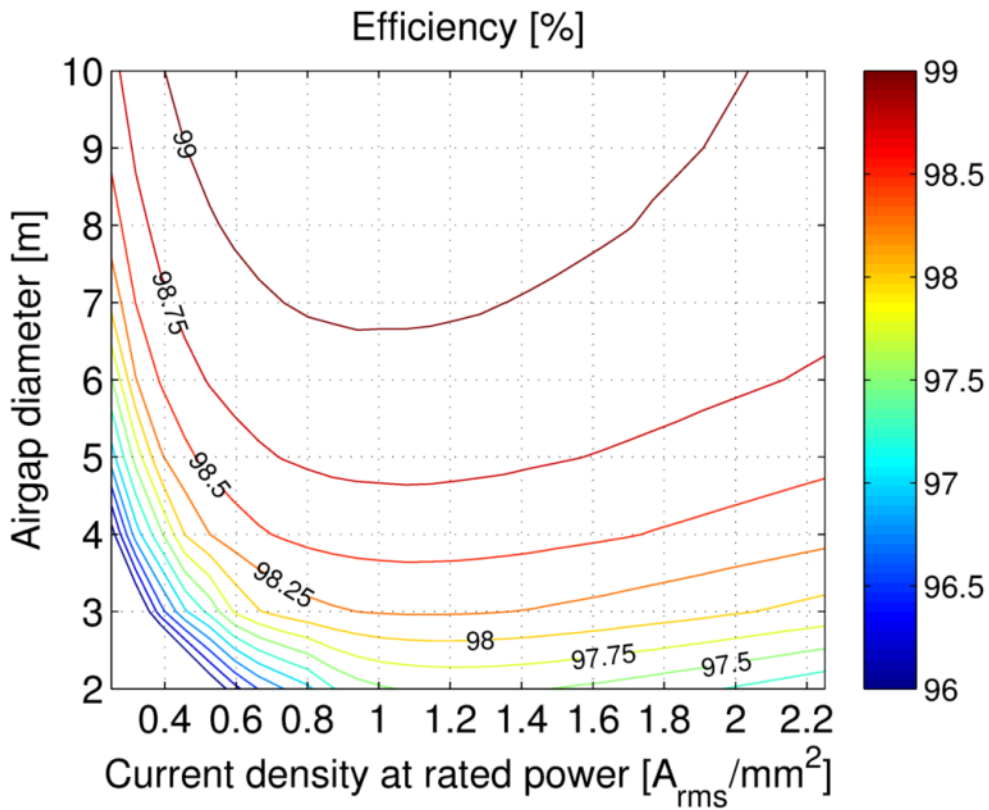


Fig. 37. Variation of rated efficiency with the airgap diameter and the current density at rated power.

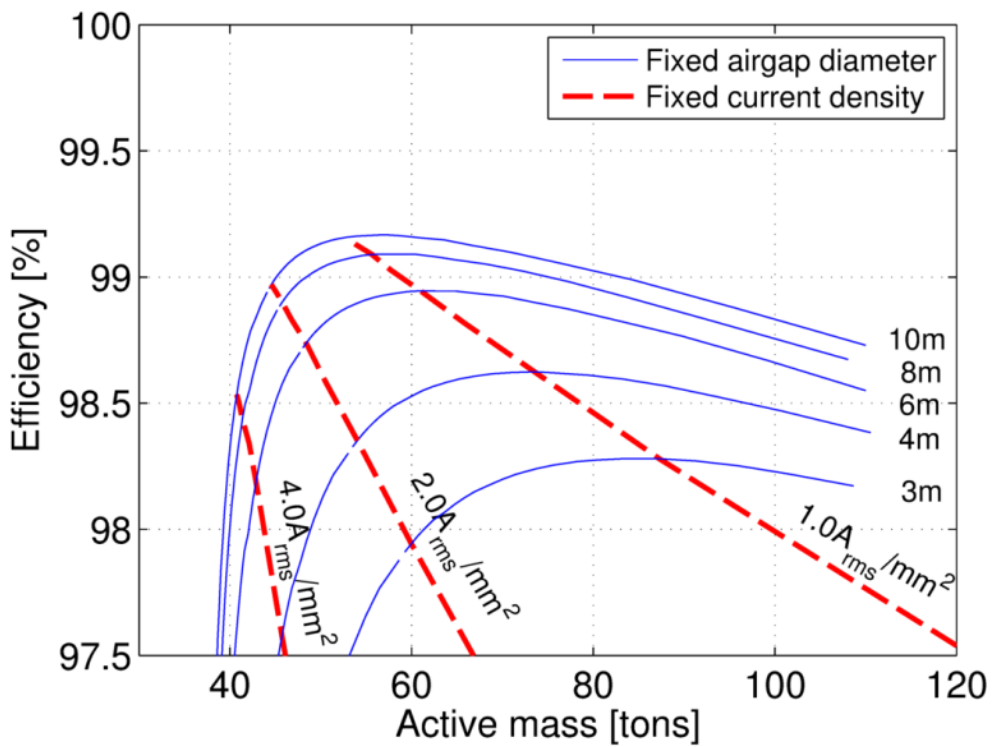


Fig. 38. Variation of rated efficiency with the total active mass for several airgap diameter.

As has been discussed in section 6.1 a wide range of number of sections, and therefore output frequencies (see equation (92)) may be considered for the PDD. Fig. 39-Fig. 41 show the variations of the PM mass, the active mass and the efficiency at rated power with the rated electrical output frequency and the achievable equivalent shear stress at pullout torque of the PDD. The gear ratio is $G=7.5$, the airgap diameter is 6.0m and the current density at rated power is $2.0A_{rms}/mm^2$. It can be seen, that for a given PM mass the equivalent shear stress varies significantly and an electrical output frequency exists, for which the shear stress is maximum.

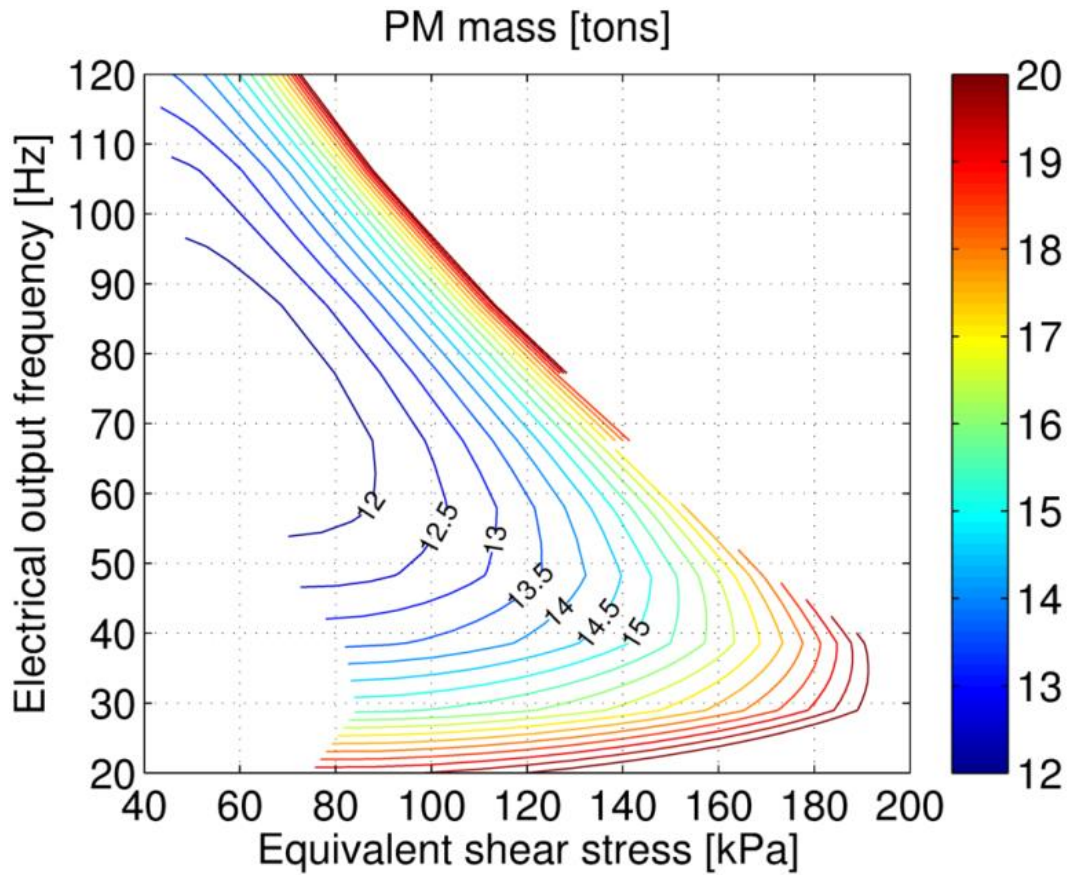


Fig. 39. Variation of PM mass with the rated electrical output frequency $f_{out,R}$ and the equivalent shear stress.

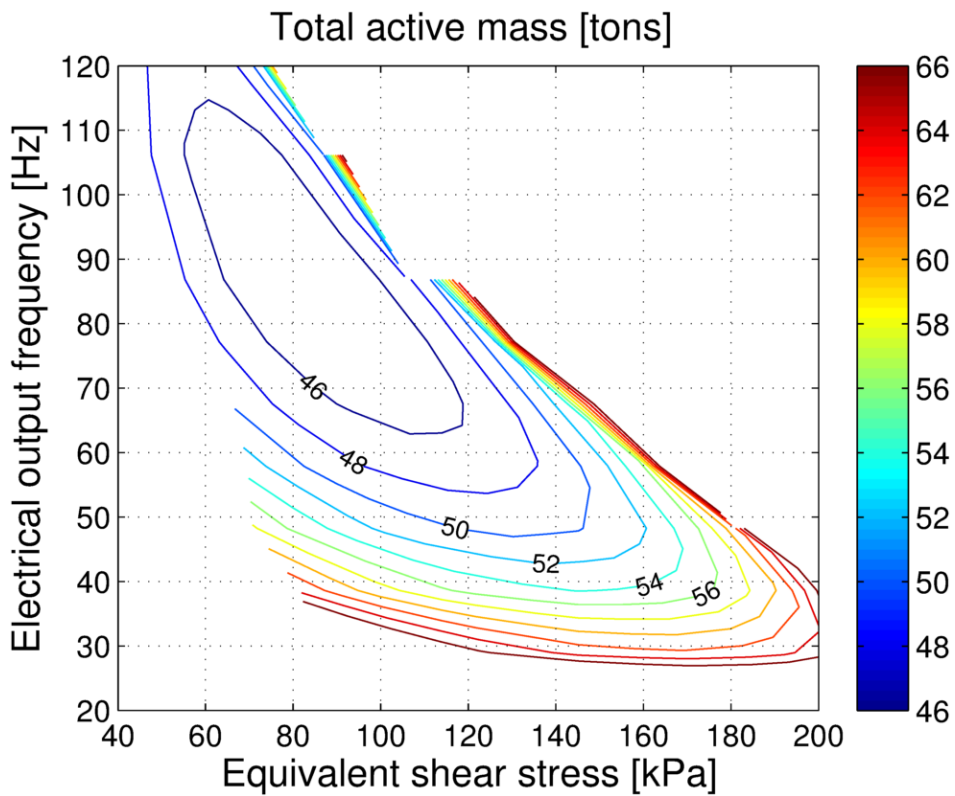


Fig. 40. Variation of total active mass with the rated electrical output frequency $f_{out,R}$ and the equivalent shear stress.

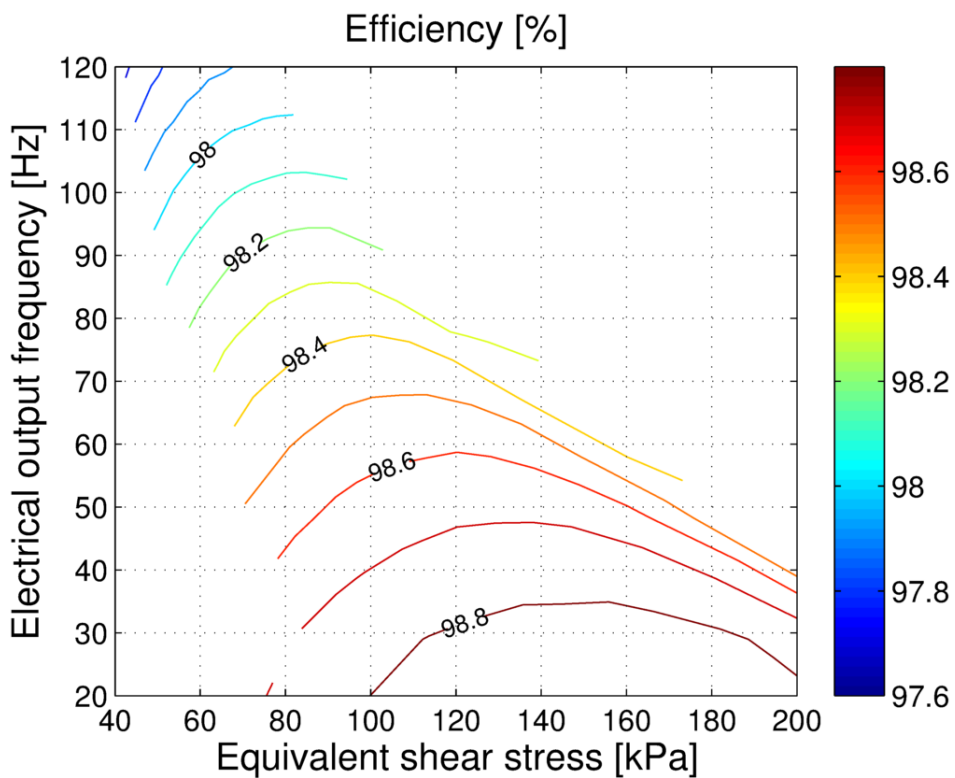


Fig. 41. Variation of efficiency with the rated electrical output frequency $f_{out,R}$ and the equivalent shear stress.

7 UP-SCALING TO 20MW

As can be seen from Fig. 34 the equivalent shear stress remains constant when increasing the airgap length, the PM width and the PP width linearly with the airgap diameter D . If also the axial length is scaled linearly with the airgap diameter the torque, the PM mass and the HS rotor and PP rotor laminated steel mass would scale with D^3 . If it is assumed, that the rotational speed scales with D^{-1} [14], the current loading Q_{rms} remains constant (see equation (82)). Furthermore, for a fixed number of poles the electrical output frequency would decrease with D^{-1} . Fig. 42 shows the variation of the various active masses with the rated power. It can be seen, that the required PM mass and laminated steel mass per unit MW increase, while the copper mass per unit MW remains constant. Fig. 43 shows the variation of the iron and copper loss per unit MW with the rated power. It can be seen, that the copper loss per unit MW remains constant, while the iron loss per unit MW decreases with increasing power rating, which is contributed towards the decreasing output frequency. Fig. 44 shows the variation of the efficiency with the rated power. It can be seen, that the efficiency improves when increasing the power rating.

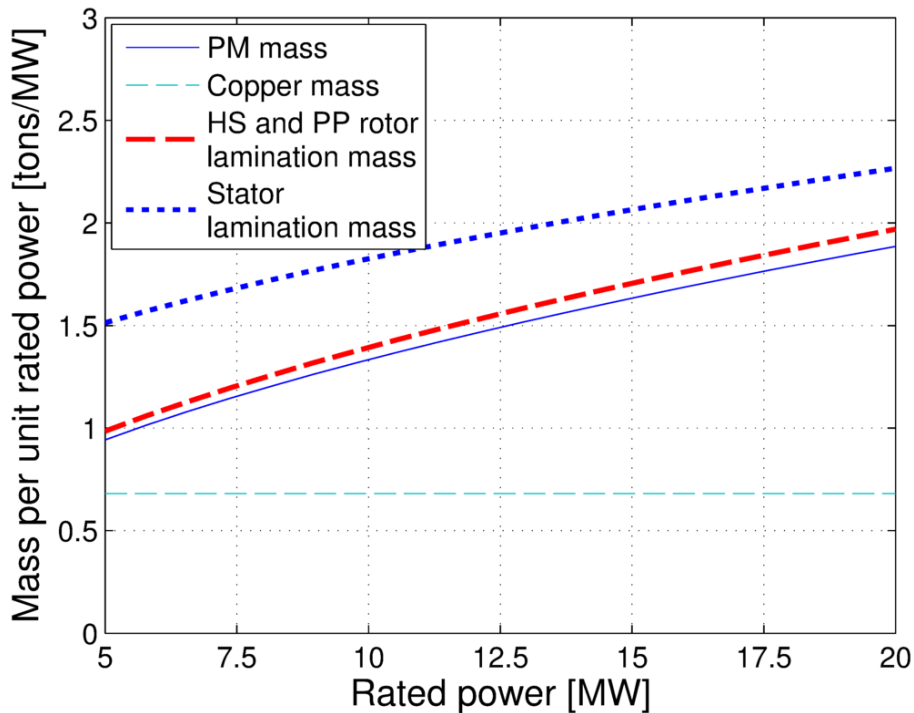


Fig. 42. Variations of the PM, copper and laminated steel mass with the rated power.

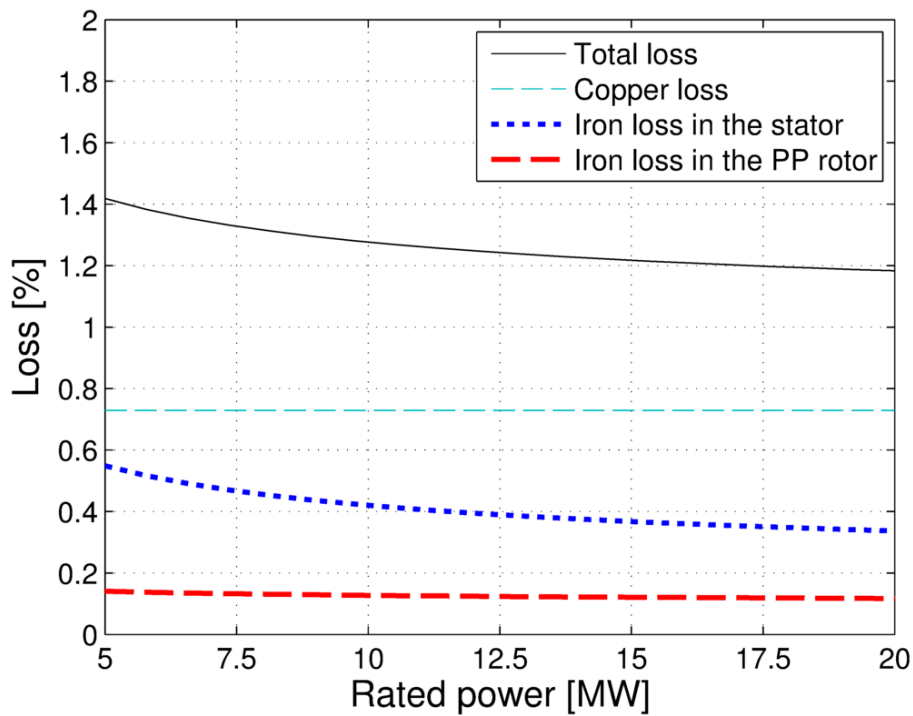


Fig. 43. Variations of copper and iron loss with the rated power.

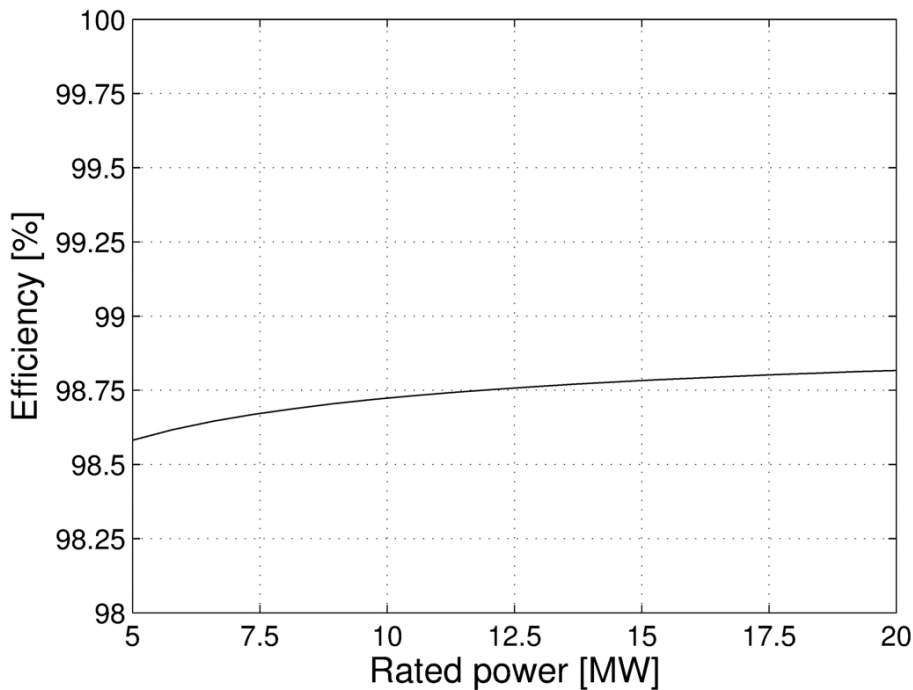


Fig. 44. Variation of efficiency with the rated power.

While up-scaling yields an initial indication on the scaling behaviour, further improvements may yet be achieved by adjusting remaining variable parameters of the PDD, such as the airgap diameter or the selected current density. Finally, the parameters for a 20MW PDD are given in Table IV after consideration of the design and optimisation procedures developed in section 6. Fig. 45 shows the variation of the efficiency for both the 10MW PDD and the 20MW PDD with the power in percent of the rated power.

TABLE IV
Parameters of 10MW and 20MW PDDs

Symbol	Quantity	Value for 10MW	Value for 20MW
	Rated power	10 MW	20MW
$\Omega_{PP,R}$	Rated speed of PP rotor	9.65 rpm	6.82 rpm
	Rated torque on the PP rotor	9.9 MNm	28.0 MNm
	Analytical pullout torque of the MG	11.9 MNm	33.7 MNm
$f_{out,R}$	Rated electrical output frequency	48.25 Hz	34.1 Hz
G	Gear ratio	7.5	7.5
p_{HS}^*	Pole-pairs on HS rotor per section	2	2
p_s^*	Pole-pairs on stator per section	13	13
m_s	Halbach segments per pole-pair on the stator	4	4
Q^*	Pole-pieces per section	15	15
S	Number of identical sections	20	20
	PP slot opening angle	$\pi/300$ rad	$\pi/300$ rad
D	Airgap diameter	6.0 m	8.5 m
w_{PP}	Radial thickness of PPs	31.4 mm	44.4 mm
	Radial thickness of HS rotor PMs	39.8 mm	56.3 mm
	Radial thickness of stator PMs	25.2 mm	35.6 mm
	Length of inner airgap	6.0 mm	8.5 mm
	Length of outer airgap	6.0 mm	8.5 mm
l_a	Active axial length	1.66 m	2.35 m
	HS rotor pole arc to pole pitch ratio	0.8	0.8
B_r	Remanence of N48SH PMs at 100°C	1.25 T	1.25 T
μ_r	Relative recoil permeability of PMs	1.05	1.05
	Copper packing factor	0.5	0.5
	Current density at rated power	2.0 A _{rms} /mm ²	2.0 A _{rms} /mm ²
	PM mass	13.5 tons	38.2 tons
	HS rotor and PP rotor laminated steel mass	14 tons	39.6 tons
	Stator laminated steel mass	15.5 tons	45 tons
	Copper mass	7 tons	14 tons
	Estimated structural mass **	100 tons	383 tons
	Estimated total mass	150 tons	520 tons

** The structural mass for the 10MW design is assumed to be 2 times the active mass, a similar factor as for the 10MW design given by Magnomatics in [15]. Furthermore, the ratio of structural mass to active mass is assumed to scale with the diameter, hence a factor of 2.8 is assumed for the 20MW design.

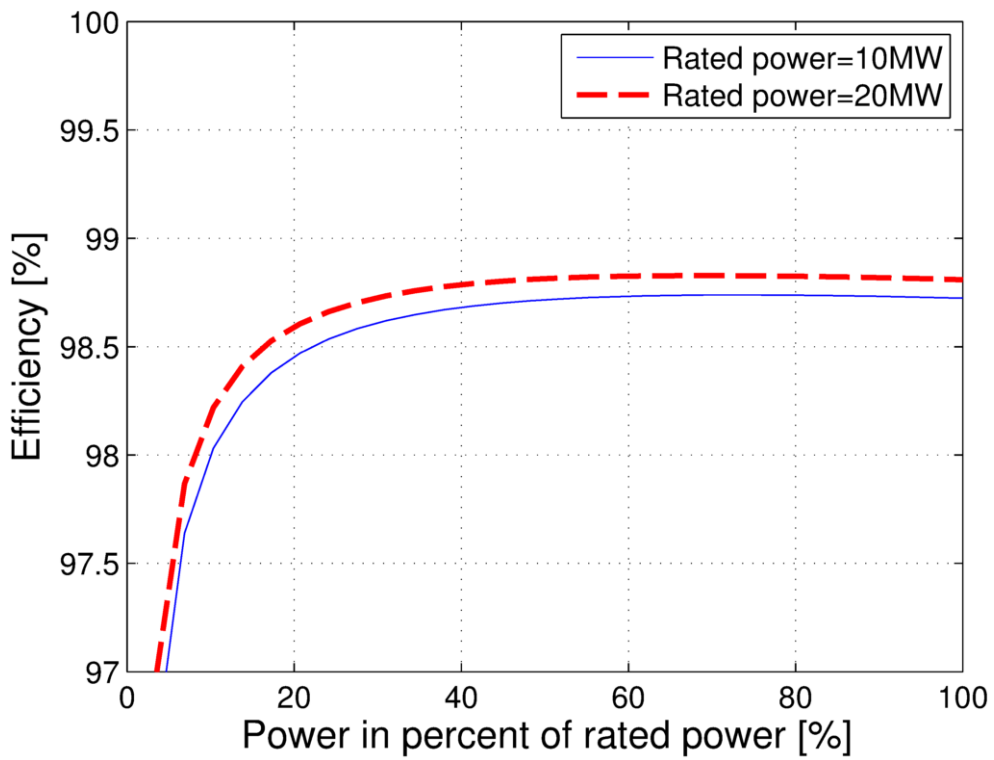


Fig. 45. Variations of the electromagnetic efficiency with the power in percent of the rated power.

8 CONCLUSION

Analytical models for the prediction of the flux density distributions in the airgap, PM and iron regions of large Pseudo-Direct Drives (PDD) are presented. It is shown, that a good agreement with 2-D finite element analysis exists for the flux density waveforms, the transmitted torque, the torque ripple and the iron loss for linear and non-linear steels. Furthermore, a good agreement also exists between analytical model and finite element for both the iron losses in the pole-pieces and the stator.

A procedure for the optimisation of large magnetic gears and PDDs has been developed and has been implemented into MATLAB code. The developed optimisation tool has been utilised for the optimisation of PDDs for a 10MW and 20MW wind turbine. It has been shown, that efficiencies above 98.5% can be achieved with a total active mass of about 50tons for a 10MW PDD and 140tons for a 20MW PDD.

9 PUBLICATIONS RESULTING FROM THE WORK

A. Penzkofer and K. Atallah, "Magnetic gears for high torque applications," *Magnetics, IEEE Transactions on*, vol. 50, no. 11, pp. 1–4, Nov 2014.

A. Penzkofer and K. Atallah, "Analytical Modelling and Optimisation of Pseudo Direct Drive Permanent Magnet Machines for Large Wind Turbines" *Magnetics, IEEE Transactions on*, Accepted for publication.

A. Penzkofer, K. Atallah, "Optimisation of magnetic gears for large wind turbines", *Environment and Electrical Engineering (EEEIC), 2015 IEEE 15th International Conference on*, vol., no., pp.962-967, 10-13 June 2015

A. Penzkofer, K. Atallah, "Coil Excited Magnetic Gears for Large Wind Turbines", Submitted to 13th Joint MMM-Intermag Conference, 11-15 January 2016

A. Penzkofer, K. Atallah, "Scaling of Pseudo Direct-Drives for Wind Turbine Applications", Submitted to 13th Joint MMM-Intermag Conference, 11-15 January 2016

References

- [1] H. Polinder, J. Ferreira, B. Jensen, A. Abrahamsen, K. Atallah, and R. McMahon, "Trends in wind turbine generator systems," *Emerging and Selected Topics in Power Electronics, IEEE Journal of*, vol. 1, no. 3, pp. 174–185, Sept 2013.
- [2] H. Tiegna, Y. Amara, and G. Barakat, "Overview of analytical models of permanent magnet electrical machines for analysis and design purposes," *Mathematics and Computers in Simulation*, vol. 90, no. 0, pp. 162 –177, 2013.
- [3] T. Lubin, S. Mezani, and A. Rezzoug, "Analytical computation of the magnetic field distribution in a magnetic gear," *Magnetics, IEEE Transactions on*, vol. 46, no. 7, pp. 2611 –2621, July 2010.
- [4] L. Jian and K.-T. Chau, "Analytical calculation of magnetic field distribution in coaxial magnetic gears," *Progress In Electromagnetics Research*, vol. 92, pp. 1–16, 2009.
- [5] L. Jian, K. T. Chau, Y. Gong, J. Z. Jiang, C. Yu, and W. Li, "Comparison of coaxial magnetic gears with different topologies," *IEEE Trans. Magn.*, vol. 45, no. 10, pp. 4526–4529, Oct. 2009.
- [6] A. Penzkofer and K. Atallah, "Magnetic gears for high torque applications," *Magnetics, IEEE Transactions on*, vol. 50, no. 11, pp. 1–4, Nov 2014.
- [7] A. Penzkofer and K. Atallah, "Analytical Modelling and Optimisation of Pseudo Direct Drive Permanent Magnet Machines for Large Wind Turbines" *Magnetics, IEEE Transactions on*, Accepted for publication.
- [8] A. Penzkofer, K. Atallah, "Optimisation of magnetic gears for large wind turbines", *Environment and Electrical Engineering (EEEIC), 2015 IEEE 15th International Conference on*, vol., no., pp.962,967, 10-13 June 2015
- [9] T. Miller and R. Rabinovici, "Back-emf waveforms and core losses in brushless dc motors," *Electric Power Applications, IEE Proceedings -*, vol. 141, no. 3, pp. 144–154, May 1994.
- [10] Atallah, K. and Rens, J. and Mezani, S. and Howe, D., "A Novel 'Pseudo' Direct-Drive Brushless Permanent Magnet Machine", *Magnetics, IEEE Transactions on Magnetics* 44, 11 (2008), pp. 4349 -4352.
- [11] K. Atallah and D. Howe, "The calculation of iron losses in brushless permanent magnet dc motors", *Journal of Magnetism and Magnetic Materials* 133 (1994), pp. 578 - 582.
- [12] H. Polinder, D. Bang, R. P. J. O. M. Van Rooij, A. McDonald, and M. Mueller, "10 MW wind turbine direct-drive generator design with pitch or active speed stall control," in *Electric Machines Drives Conference, 2007. IEMDC '07. IEEE International*, vol. 2, 2007, pp. 1390–1395.
- [13] A. Zavvos, A. McDonald, and M. Mueller, "Structural optimization tools for iron cored permanent magnet generators for large direct drive wind turbines," in *Renewable Power Generation (RPG 2011), IET Conference on*, Sept 2011, pp. 1–6.
- [14] G. Sieros, P. Chaviaropoulos, J. D. Sørensen, B. H. Bulder, and P. Jamieson, "Upscaling wind turbines: theoretical and practical aspects and their impact on the cost of energy," *Wind Energy*, vol. 15, no. 1, pp. 3–17, 2012.
- [15] Dong Liu, A. B. Abrahamsen, H. Polinder, et. al., "Deliverable D3.42 First assessment of performance indicators of SC and PDD generators", INN WIND.EU, WP3 internal report, Sept 2013.

APPENDIX A: ELECTRICAL PARAMETERS OF THE OPTIMISED 10MW PDD

Values have been calculated for the rated rotational speed of the pole-piece rotor of $\omega_{PP} = 9.65 \text{ rpm}$. The number of turns per coil N has been chosen to be $N=1$ and the respective electrical parameters for a 10MW PDD are shown in Table 1.

TABLE V
Parameters of a 10MW PDD

Symbol	Quantity	Value
ω_{PP}	Rated speed of PP rotor (wind turbine rotor)	9.65 rpm
G	Gear ratio	7.5
ω_{HS}	Rated speed of high-speed rotor	72.4 rpm
p_{HS}	High-speed rotor pole-pairs	40
f	Excitation frequency	48.25 Hz
E_C	EMF/turn/coil	24.0 V _{rms}
R_C	Resistance/turn/coil	24.6 $\mu\Omega$
L_C	Self-inductance/turn/coil	7.55 μH
M_C	Mutual inductance/turn (between 2 consecutive coils)	-3.56 μH

However, it is expected that N has to be modified to suite the requirements of the application and the following quantities can then be calculated as follows:

$$\text{EMF/coil:} \quad E = N E_C \quad (1)$$

$$\text{Resistance/coil:} \quad R = N^2 R_C \quad (2)$$

$$\text{Self-inductance/coil:} \quad L = N^2 L_C \quad (3)$$

$$\text{Mutual inductance/coil:} \quad M = N^2 M_C \quad (4)$$

Example electrical connection and calculation of circuit parameters:

Fig. 46 shows a possible configuration for the generator feeding K converters. The number of series coils per phase per converter would be p_{HS}/K . The parameters of the phases feeding the converters are then given by:

$$\text{EMF/phase:} \quad E_p = N E_C \left(\frac{p_{HS}}{K} \right) \quad (5)$$

$$\text{Resistance/phase:} \quad R_p = N^2 R_C \left(\frac{p_{HS}}{K} \right) \quad (6)$$

$$\text{Self-inductance/phase:} \quad L_p = N^2 L_C \left(\frac{p_{HS}}{K} \right) \quad (7)$$

$$\text{Mutual inductance/phase:} \quad M_p = N^2 M_C \left(\frac{p_{HS}}{K} \right) \quad (8)$$

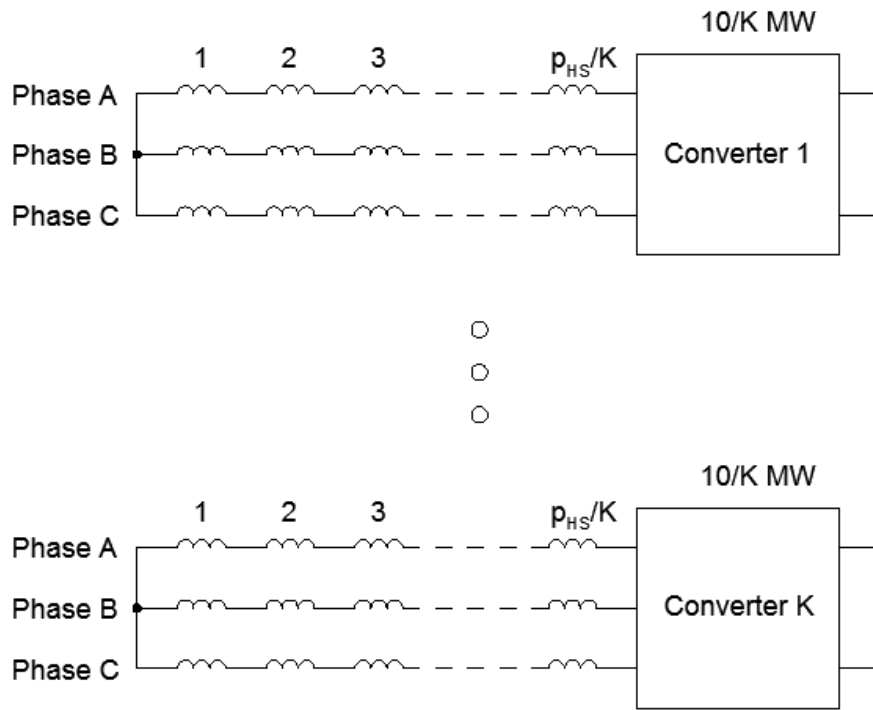


Fig. 46. Schematic for a 10MW Generator with K converters.

APPENDIX B: ELECTRICAL PARAMETERS OF THE OPTIMISED 20MW PDD

Values have been calculated for the rated rotational speed of the pole-piece rotor of $\omega_{PP} = 6.82 \text{ rpm}$. The number of turns per coil N has been chosen to be $N=1$ and the respective electrical parameters for a 20MW PDD are shown in Table 1.

TABLE VI
Parameters of a 20MW PDD

Symbol	Quantity	Value
ω_{PP}	Rated speed of PP rotor (wind turbine rotor)	6.82 rpm
G	Gear ratio	7.5
ω_{HS}	Rated speed of high-speed rotor	51.15 rpm
p_{HS}	High-speed rotor pole-pairs	40
f	Excitation frequency	34.1 Hz
E_c	EMF/turn/coil	33.9 V _{rms}
R_c	Resistance/turn/coil	24.6 $\mu\Omega$
L_c	Self-inductance/turn/coil	9.96 μH
M_c	Mutual inductance/turn (between 2 consecutive coils)	-4.57 μH

